SANDIA REPORT
SAND2018-10651
Unlimited Release
Printed September 2018

LDRD 200166: In-Cylinder Diagnostics to Overcome Efficiency Barriers in Natural Gas Engines

Mark PB Musculus, Judit Zador, Zheming Li, Ken Stewart, Dave Cicone, Greg Roberts

Prepared by Mark PB Musculus
Sandia National Laboratories
Albuquerque, New Mexico 87185 and Livermore, California 94550

Sandia National Laboratories is a multimission laboratory managed and operated by National Technology and Engineering Solutions of Sandia, LLC, a wholly owned subsidiary of Honeywell International, Inc., for the U.S. Department of Energy's National Nuclear Security Administration under contract DE-NA0003525.

Sandia National Laboratories

Issued by Sandia National Laboratories, operated for the United States Department of Energy by National Technology and Engineering Solutions of Sandia, LLC.

Available to DOE and DOE contractors from
U.S. Department of Energy
Office of Scientific and Technical Information
P.O. Box 62
Oak Ridge, TN 37831

Telephone: (865) 576-8401
Facsimile: (865) 576-5728
E-Mail: reports@osti.gov
Online ordering: http://www.osti.gov/scitech

Available to the public from
U.S. Department of Commerce
National Technical Information Service
5301 Shawnee Rd
Alexandria, VA 22312

Telephone: (800) 553-6847
Facsimile: (703) 605-6900
E-Mail: orders@ntis.gov
Online order: https://classic.ntis.gov/help/order-methods/

SAND2018-10651
Printed September 2018
Unlimited Release

LDRD 200166: In-Cylinder Diagnostics to Overcome Efficiency Barriers in Natural Gas Engines

Mark Musculus (8362), Judit Zador (8353), Zheming Li (8362),
Ken Stewart (8367), Dave Cicone (8362), Greg Roberts (8362)

8362 – Engine Combustion; 8353 – Combustion Chemistry;
8367 – Hydrogen & Materials Science

Sandia National Laboratories
P. O. Box 5800
Albuquerque, New Mexico 87185

Abstract

The high-level objective of this project is to solve national-security problems associated with petroleum use, cost, and environmental impacts by enabling more efficient use of natural-gas-fueled internal combustion engines. An improved science-base on end-gas autoignition, or "knock," is required to support engineering of more efficient engine designs through predictive modeling. An existing optical diesel engine facility is retrofitted for natural gas fueling with laser-spark-ignition combustion to provide in-cylinder imaging and pressure data under knocking combustion. Zero-dimensional chemical-kinetic modeling of autoignition, adiabatically constrained by the measured cylinder pressure, isolates the role of autoignition chemistry. OH* chemiluminescence imaging reveals six different categories of knock onset that depend on proximity to engine surfaces and the in-cylinder deflagration. Modeling results show excellent prediction regardless of the knock category, thereby validating state-of-the-art kinetic mechanisms. The results also provide guidance for future work to build a science base on the factors that affect the deflagration rate.

ACKNOWLEDGMENTS

The authors acknowledge and thank former Sandia National Laboratories post-doc W. Ethan Eagle and visiting researcher Christine Rousselle from CNRS Orleans for their advice and contributions in the early stages of this project. The contributions of technologist Alberto Garcia to the design and construction of the acetone vaporizing system are also acknowledged and appreciated. Gratitude is also extended to managers Paul Miles and Chris Moen for supporting the work and helping to complete the necessary technical work documentation so that experiments could proceed. Finally, the director of center 8300, Bob Hwang, was instrumental in providing critical support to this project through his efforts to ensure that the resources and highly qualified personnel required for the considerable design and hardware construction portions of the project were available.

TABLE OF CONTENTS

FIGURES

TABLES

NOMENCLATURE

Abbreviation	Definition
0-d	Zero dimensional (model)
AHRR	Apparent heat release rate
ºCA	Degrees crank-angle (temporal duration measured in crank-angle space)
CAD	Crank angle degree (360 CAD is top-dead-center of compression stroke)
CMOS	Complementary metal oxide semiconductor
GDI	Gasoline direct injector
HPDI	High-pressure direct injection
OH*	Excited-state hydroxyl radical
RPM	Rotations per minute
UV	Ultraviolet

1. MOTIVATION AND OBJECTIVES

Abundant domestic natural gas resources (fossil plus renewable) could help achieve the United States Department of Energy's energy-security and greenhouse-gas emission goals, but only if natural gas could be used more broadly in transportation, especially in heavy-duty trucking. Unfortunately, current state-of-the-art natural gas engines, which use spark-ignition, fall well short of diesel fuel-efficiency, such that fuel-cost economics severely limit natural gas market penetration. The primary barrier to higher spark-ignition natural gas efficiency is end-gas autoignition, or "knock," which limits the engine compression ratio. Deficiencies in the science base for spark-ignition natural gas engine combustion hinder the predictive accuracy of computer-modeling tools that could otherwise yield more efficient, knock-tolerant engine designs.

In the following sections, further details of the technical background that motivates the project is described, followed by the objectives for the experimental and computer modeling efforts.

1.1. Technical Background

As of August 2018, 71% of US petroleum is used for transportation [1], and approximately 50% (gross) is imported (35% exports, 15% net imports) [1,2]. Increased fueling of ground transportation engines with domestically produced fossil or renewable natural gas would help meet two major United States Department of Energy goals: increased energy security by displacing imported petroleum, and reduced greenhouse-gas emissions, with an estimated 20-30% reduction relative to gasoline fueling [3-5][*]. Historical natural gas economics often have been favorable as well – from 2010 to 2015, the energy-equivalent cost of natural gas was 30-45% lower than gasoline [6]. The price volatility during this period was also lower for natural gas, with variations of only ±6% compared to ±33% for gasoline [6], which is an important consideration for commercial fuel budget planning, and hence can be an additional market advantage for natural gas.

An important factor limiting natural gas engine market penetration is its thermal efficiency [7]. Spark-ignition natural gas thermal efficiency is competitive with gasoline, but is ~15% lower than diesel [3], which is commonly used in fleets, currently the largest US natural gas engine market. End-gas autoignition, or "knock," limits the maximum compression ratio, and hence efficiency [8]. Natural gas engines can use cooled exhaust-gas recirculation to extend the knock limit to enable higher compression ratios [9], but tradeoffs like misfire and slower flame speed reduce thermal efficiency and can increase pollutant emissions [8].

With sufficient understanding of the in-cylinder physical and chemical processes affecting knock, and with corresponding computer modeling tools based on that understanding, engine designs could be optimized to extend the knock limit and

[*] Although greenhouse-gas reductions relative to gasoline (mostly light-duty automotive) engines are considerable, anticipated greenhouse-gas reductions for current spark-ignition natural gas engines are approximately flat relative to diesel engines in the heavy-duty sector [5].

achieve higher efficiency without undesirable combustion tradeoffs. Unfortunately, the current understanding of in-cylinder natural gas ignition, combustion, and autoignition processes available to the natural gas engine manufacturing industry is insufficient to further optimize engine designs [10].

By contrast, our understanding of diesel combustion has greatly advanced in recent decades [11,12], due in large part to Sandia's optical engine studies with laser-based and/or imaging diagnostics. Combined with improved flow, spray, and chemical-kinetics models, this understanding forms the foundation for optimization of modern diesel engines, especially through simulation tools based on that understanding. A recent study found that this type of research and consequent improvement of computer modeling tools for engine design yielded a 75-fold payoff in fuel and health effects savings [13]. Optical-engine research on natural gas combustion is comparatively sparse, however, with only 45 natural gas optical-engine studies in the Society of Automotive Engineers literature, compared to 795 for diesel. Expanding the natural gas science base with improved understanding of knock limitations to efficiency will support engine design and engineering efforts to build more efficient engines. If natural gas engines can gain even half of the 30% efficiency improvements realized in diesel engines over the years of optical diesel engine research [14], the resulting diversification of national transportation engine options would be transformational.

1.2. Experimental and Modeling Objectives

The strategic objectives of this project are to leverage Sandia's proven experimental and modeling expertise to develop deeper fundamental understanding of in-cylinder processes of natural gas engines. This project addresses knock in stoichiometric spark ignition natural gas engines to achieve higher thermal efficiency, including fundamental chemistry improvements for engine-design simulation tools.

The first technical objective is to retrofit an existing optical diesel engine facility for natural gas fueling with laser-spark-ignition combustion to provide in-cylinder imaging and pressure data under knocking combustion. Then, using the measured cylinder pressure as a constraint on a simplified zero-dimensional chemical-kinetic model, images of OH* chemiluminescence from the experiments can provide guidance on whether or not the adiabatic assumption of the model is justified for any particular knocking cycle. This combination of experimental and modeling objectives is designed specifically for this problem, as it allows chemical kinetics to be decoupled from complex in-cylinder physical processes in a way not generally possible in engines. A further objective is to use comparisons between model predictions and experimental measurements to gain insight into the in-cylinder physical and chemical processes that complicate predictions of the onset of knock, which will provide guidance on how to improve computer modeling tools so that they can be utilized for designing more efficient engines.

2. EXPERIMENTAL FACILITIES AND MODELS

This experiment uses a previously existing optical heavy-duty diesel engine that is retrofit for natural-gas fueling as part of this project. A natural gas fuel source system that delivers and recovers certification-grade natural gas mixtures to the laboratory at pressures up to 650 bar that was built as part of this project to support the engine experiments is described in Section 2.1. A new natural gas fuel delivery system with three independent and simultaneously functional legs to deliver natural gas to three different fuel injection systems at three different supply pressures is described in Section 2.2. A new acetone vaporizer system for seeding the natural gas fuel stream with acetone for fuel-tracer diagnostics is described in Section 2.3. The existing optical heavy-duty diesel engine and retrofits for natural gas fueling that were implemented as part of this project are described in Section 2.4. The engine operating conditions and optical diagnostics for the experimental data that were acquired as part of this project are described in Section 2.5. The 0-d model and associated chemical kinetics mechanisms are described in Section 2.6.

2.1. Natural Gas Fuel Source System

Several constraints on the experimental design for this project require a specialized natural gas fuel source system. First, the companion modeling effort requires precise definition of the natural gas fuel for accurate predictions. The composition of utility-grade natural gas varies from region to region and from time to time, sometimes with variations that cause observable changes to engine operation over the course only a few minutes [15]. Hence, sufficient storage of an unchanging natural gas supply is required. Because minor constituents in natural gas, such as longer-chain hydrocarbons, play such an important role in the chemical kinetics of knock [16], the composition of the natural gas must be precisely set. Two options that merit consideration are 1) on-site, on-the-fly mixing of individual natural-gas components, and 2) using pre-defined mixtures of natural-gas components, certified by a specialty gas supplier.

The first option requires significant investment in either multiple gas-supply legs for each of the individual components, or single common delivery leg for batch processing of each of the individual components. Either case requires calibration of the delivered quantity of each individual component and/or characterization of the composition after mixing of the individual components. Such capabilities would require considerable investment in a mixing system capable of reducing the uncertainty in the composition from batch to batch to acceptable levels.

The second option avoids this expense, relying instead on the already existing gas mixing and characterization infrastructure of commercial specialty gas suppliers. While the expense and lead-time of certified natural gas mixtures from a specialty gas supplier is greater than the material costs of in-house mixing, the in-house infrastructure costs are prohibitively high. Hence, the second option was selected.

The expensive, long lead-time certified gas mixtures introduce a further constraint on the system to minimize waste of the natural gas fuel. Experimental operations unavoidably require depressurizing parts of the system for maintenance or safety.

Depressurization by venting would waste the expensive certified gas mixtures, so the system was design with a compression system for gas recovery into separate pressurized storage cylinders.

A further constraint on the system is the need for natural gas delivery to the engine at pressures up to 600 bar for the future HPDI system on the engine. The natural gas supply system would need to generate even higher pressures that would be regulated down to the desired 600-bar pressure at the engine. Pressures of 600 bar or more exceed those of available commercial specialty gases (typically 170 bar), so a gas compression system to increase the pressure of the commercial cylinders to that required for engine operation is required.

The dual-compressor natural gas fuel source system that was designed and built as part of this project to both pressurize the natural gas as required for engine operation and to recover the natural gas into storage for future use is located in the flammable gas station on the dock of laboratory space 165 in building 906 of the California site. Shown in Figure 1 is a schematic of the system, and a list of the numbered components is available in [17]. The following is a description of the key design, operation, and safety features of the natural gas fuel source system.

The natural gas source system is divided into four distinct functional subsystems: 1) a source cylinder of compressed natural gas and the associated control system; 2) a high-pressure compressor system to increase the pressure from the commercial certified natural gas cylinder to the pressure required for the natural gas delivery system described in Section 2.2, and with an accumulated volume sufficient to provide pressurized natural gas over the duration of an experimental run; 3) a low pressure compressor and storage tanks to recover natural gas from the source system and/or from the delivery system; and 4) a rough vacuum system for pump-down of the system to facilitate changing to different natural gas compositions, removing impurities from the system, and/or for leak checking. The functionality and safety considerations for each subsystem is described individually in the following subsections, with key components from the schematic in Figure 1 identified within curly brackets. See [17] for a full listing of all components.

2.1.1. Natural Gas Source Cylinder and Control Subsystem

The natural gas source cylinder {1} in Figure 1 is 1A size, and provides certified mixtures of natural gas purchased from a specialty gas vendor, pressurized up to approximately 160 bar-g (2300 psig). These gas mixtures are primarily methane (typically 80-95% by volume) with the balance typically composed of ethane, propane, butane, nitrogen, carbon monoxide and/ or carbon dioxide. For some experiments, standard-reference natural gas mixtures composed of methane and hydrogen may be used, with hydrogen content up to 20% by volume.

From the supply cylinder {1}, the natural gas passes through a check valve {3}, an optional restrictive flow orifice {4}, and a filter {7} before being regulated down by a pressure regulator {8} to 31 bar-g (450 psig), the nominal inlet pressure of the high-pressure compressor {60} at the high-pressure compressor suction line {16}. The check valve {3} prevents backward flow into the source cylinder {1} of atmospheric

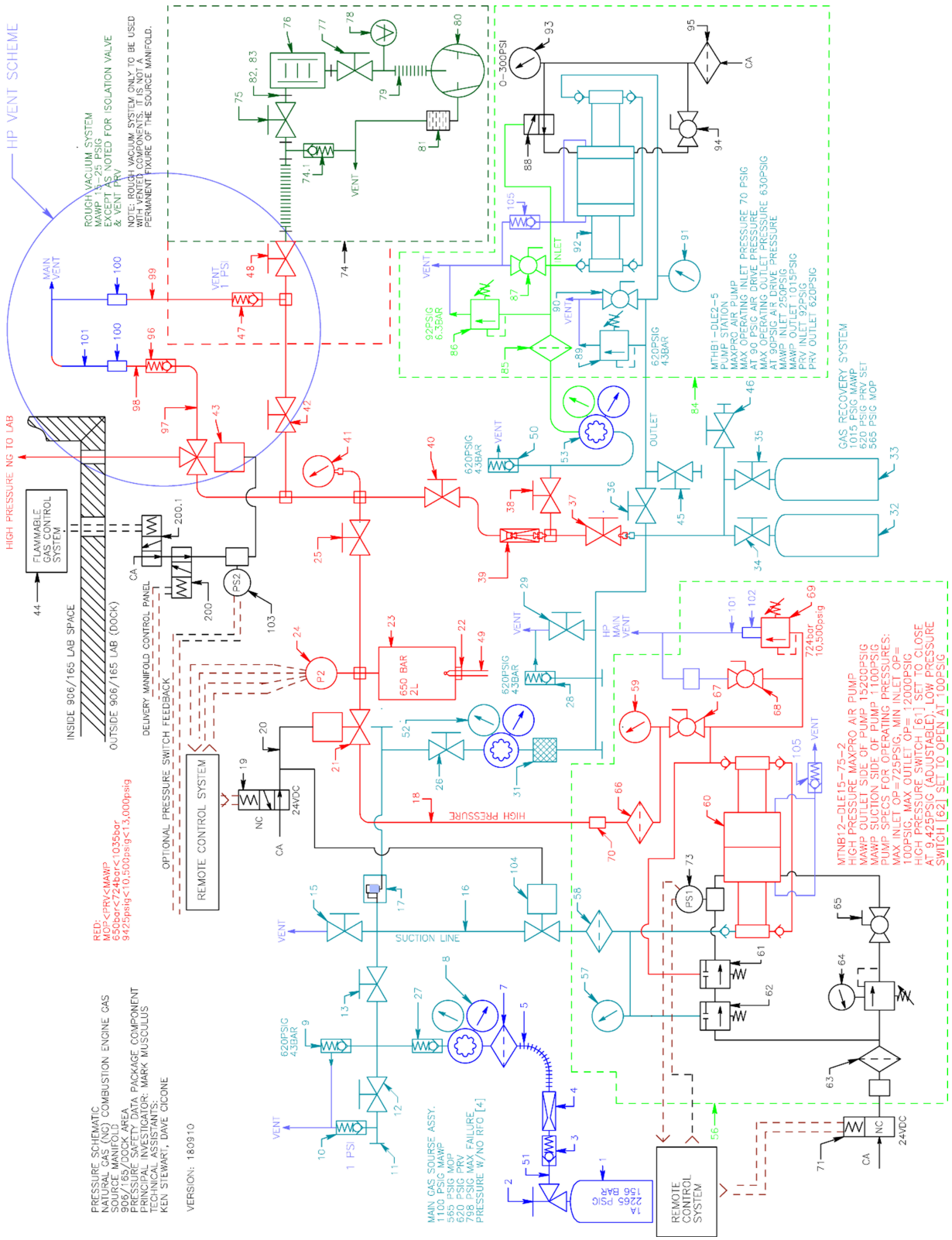

Figure 1. Schematic of natural gas fuel source system. See [17] for component list.

gases that would otherwise enter the manifold during cylinder changes when the connection between the supply cylinder valve {2} and the check valve {3} is opened.

The lift check valve {17} prevents natural gas from flowing from the high-pressure compressor suction line {16} into the recovery system (described in Subsection 2.1.3). The pressure relief valve {9} is set to 43bar (620psig), which will yield an maximum back pressure of 800 psig at the calculated [17] flow rate of that would result from failure of the regulator {8}. The high-pressure compressor can tolerate up to 1100 psig on the suction line {16}, so the 800 psig maximum pressure provided by the pressure relief valve {9} is sufficient to protect the high-pressure compressor from damage. Hence, for the current configuration, the optional restrictive-flow orifice {4} is not necessary, and is also not desirable because the restriction limits the rate at which the natural gas can be emptied from the source cylinder {1} before the high-pressure compressor {60} has insufficient inlet supply pressure at its flow capacity.

2.1.2. High-Pressure Compressor Subsystem

The natural gas fuel delivery system described in Section 2.2 requires natural gas pressures of up to 600 bar at the engine. The flow rate of the high-pressure compressor {60} is insufficient to satisfy the needs for fueling the engine during an experimental run, so prior to the start of an experiment, natural gas must be accumulated at a pressure sufficiently high to maintain up to 600 bar-g natural gas pressure at the engine as the accumulated volume is depleted as it supplies natural gas to the engine. Based on the needs of the experiments, an accumulated volume of 2 liters of the source accumulator {23} would need to be pressurized 50 bar (725 psi) above the desired pressure at the engine to provide sufficient stored natural gas for the duration of an experimental run so that the pressure in the source accumulator {23} does not drop below the desired pressure at the engine. Hence, the natural gas must be pressurized to as much as 650 bar-g (9425 psig).

Natural gas is delivered by the source cylinder system of Subsection 2.1.1 to the suction line {16} of the high-pressure compressor {60}, which is a reciprocating piston design that is powered by compressed air. It pressurizes the natural gas in two stages, starting from a suction pressure of 7-31 bar-g (100-450 psig) to an outlet pressure of up to 650 bar-g (9425 psig). The maximum operating pressure on the suction line {16} is specified by the compressor manufacturer to be five times the compressed air pressure. If the maximum operating pressure on the suction line is exceeded, the pump stalls, but it is not damaged until the maximum allowable working pressure of 1100 psig is exceeded. With a typical building compressed air pressure of 6.2 bar-g (90 psig), the maximum operating pressure is 31 bar-g (450 psig). Hence, the supply regulator {8} is typically set to 450 psig, while the pressure relief valves {9, 14, 28, and 89} are set a large margin above the maximum operating pressure, at 620 psig. The large margin helps to avoid unnecessary venting of expensive natural gas in the event that the maximum operating pressure, but not the maximum allowable working pressure, is exceeded. The inlet natural gas comes from either the source cylinder {1} or from the recovery tanks {32, 33} of the natural gas recovery system, as described in the Subsection 2.1.3. The compressed air inlet on the high-pressure compressor is rated by the manufacturer for 1-10 bar-g (15-145 psig), while the

building compressed air has a maximum pressure of only 7 bar-g (100 psig). Therefore, there is no requirement for pressure relief on the compressed air line to the high-pressure compressor.

Within the high-pressure compressor assembly {56}, the compressed air line is split into two legs, one for each of the two pistons. When the high-pressure compressor is operating, the natural gas pressure in the outlet line {18} rises as downstream components in the natural gas source system and the delivery system are filled. The output flow from the high-pressure compressor will continue to slow down as the outlet pressure rises due to decreasing volumetric efficiency, as described in the certification section of the compressor technical data sheet [18]. During this pump-up process, the high-pressure compressor system will automatically cease actuation in two different situations, using on-board factory switches. First, if the outlet reaches its target pressure, nominally 650 bar-g (9425 psig), the on-board output pressure switch {61} shuts off the compressed air pilot flow. Second, the suction line {16} is also plumbed into the air pilot pressure switch {62}. This switch senses the natural gas suction pressure to the high-pressure compressor and will shut down the compressed-air pilot flow if the natural gas inlet pressure falls below the minimum pressure setting of 7 bar-g (100 psig). This underscores the design intent to avoid using the optional restrictive flow orifice {4} in the natural gas source control system of Subsection 2.1.1.

In addition to the automatic shut-off function actuated by the on-board pressure switches {61 and 62}, the high-pressure compressor {60} may be shut down remotely from inside the lab, either automatically or manually, from a control panel inside the lab. To inform operators of the current system pressure so that they may decide if remote shut-down is necessary, the pressure in the natural gas source accumulator {23} is monitored in the lab by a pressure transducer {24}. Using a read-out inside the lab, the natural gas pressure in the accumulator outside the lab is always known at a glance to users inside the lab. The pump status is monitored in the lab through a feedback signal from pressure switch {73} installed onto the compressed air line after the low-pressure {62} and high-pressure {61} switches that control compressed air delivery to the pilot valve of the high-pressure compressor. This switch will open if compressed air is below ~70 psig (adjustable) indicating that compressed air is not supplied to the pilot valve, and the compressed-air solenoid valve {71} will close automatically (compressor off). In addition, the read-out is interfaced with control of the compressed-air solenoid {71} that supplies compressed air both to the high-pressure compressor and to the compressed air solenoid {19} that opens the valve from the high-pressure output line of the pump {18} to the accumulator volume {23}. The desired high-pressure setpoint is entered into the controller on the control panel inside the lab. Once the setpoint is reached, the controller automatically closes both of the solenoid valves {71 and 19}, shutting off the high-pressure compressor and isolating it from the accumulator volume {23}.

When the accumulators in both the natural-gas supply and delivery systems all reach their respective set pressure as indicated by the pressure reading (at set-point value), the high-pressure pump will shut down automatically, as described above, and with restart when the pressure in the accumulator volume {23} drops a selectable margin

below the setpoint (typically 5 bar). If desired, the operator may also shut down the compressor and prevent restart from the control panel, while also isolating the accumulator {23} from the high-pressure outlet of the compressor {18}. If an operator decides to shut down the pump remotely (from the inside lab space) at any time, the operator uses switches on the control panel to close the source accumulator valve isolation valve {21} and closes the compressed solenoid valve {71}, which shuts off the compressed air flow and stops the pump and prevents it from restarting automatically.

The high-pressure compressor may also be shut down manually at the compressor itself. There are two dial pressure indicators {41 and 59} to inform operators of the system state. To manually shut the compressor down at the source, the compressed air line is closed using the manual isolation valve {65}, and the source accumulator {23} may be isolated from the high-pressure compressor by closing the high-pressure natural gas output manual valve {67}.

Based on the 650 bar-g (9425 psig) requirement for the natural gas delivery system of Subsection 2.1.3, the components on the outlet side of the high-pressure pump {60} are assigned a maximum operating pressure of 650 bar-g (9425 psig). The maximum allowable working pressure of the source system on the outlet side of the high-pressure compressor {60} is determined by the lowest-pressure-rated component, which is the source accumulator {23}, with a maximum allowable working pressure of 900 bar-g (13,000 psig). At a compressed air pressure of 6 bar-g (90 psig), the output pressure capability of the high-pressure compressor is inherently limited to 830 bar-g (12,000 psig). Therefore, the high-pressure compressor outlet side of the natural gas source system does not strictly need over-pressure protection. Nevertheless, since the maximum operating pressure is only 650 bar-g (9425 psig), a pressure relief valve {69} is installed on the output side of the high-pressure compressor and is set to 724 bar-g (10,500 psig), which is then the maximum output pressure of the high-pressure compressor {60}.

An important safety feature of the system is the three way valve {43} that ties the natural gas source manifold outside the lab to the natural gas delivery manifold of Subsection 2.2, which is inside the lab. This is the ultimate shut-off device for isolating the natural gas source manifold outside the lab from the natural gas delivery manifold inside the lab, for instance during an emergency. This valve is interlocked with the building flammable gas detection system. As described in the 906/165 lab standard operating procedure [19], the flammable gas safety system automatically closes this valve if the flammable gas concentration inside the lab exceeds 10% of the lower explosion limit. When this three-way valve {43} is de-energized, it opens the natural gas delivery manifold components to the roof vent, thereby blowing down the natural gas delivery manifold (Subsection 2.2) inside the lab. The three-way valve {43} can also be deactivated remotely using the safety system control panel inside the lab, which will blow down the natural gas delivery system inside the lab in the same way. This allows the operators an immediate response to safely de-energize the lab from stored pressure during an unsafe situation that does not necessarily trigger the building flammable-gas detection system.

2.1.3. Low-Pressure Recovery and Storage Subsystem

The low-pressure recovery system transfers natural gas out of the natural gas source (Section 2.1) and delivery (Section 2.2) systems and into two parallel natural gas recovery/storage tanks {32 and 33}, which are Sandia-owned, size 1A cylinders. Combined they provide an internal volume of 87.6 L with an maximum allowable working pressure of 207 bar-g (3000 psig).

When a series of experiments with a particular natural mixture is completed, or when the supply and/or delivery systems need to be depressurized for maintenance or safety, the current natural gas mixture will need to be removed from the systems. In addition to the pressurized components of the supply system already described above, the three accumulators in the natural gas delivery system of Section 2.2 may be pressurized at up to 600 bar-g (8700 psig), 100 bar-g (1450 psig), and 10 bar-g (145 psig). Additionally, if the recovery tanks {32 and 33} of this natural gas recovery system have been used in a previous recovery operation, they will have some existing pressure, typically a minimum of 7 bar-g (100 psig) residual natural gas (the minimum high-pressure pump inlet pressure). Depending on the needs of the recovery operation, the natural gas in all of these volumes may need to be added to the recovery tanks {32 and 33}.

A typical recovery operation begins with a blow-down of the high-pressure parts of the system into the recovery tanks {32 and 33}. If only the natural gas delivery manifold inside the lab is to be emptied, then the source accumulator manual isolation valve {25} can be closed to isolate the source accumulator {23} from the recovery tanks {32 and 33}. Then, four other isolation valves {34, 35, 37, and 40} between the high-pressure system (depicted in red in Figure 1) and the recovery tanks {32 and 33} may be opened. In the natural gas delivery manifold inside the lab, all of the lab accumulator valves are also opened so that all of the natural gas in the delivery manifold is expanded into the storage tanks {32 and 33}.

Once the pressure in the natural gas delivery manifold inside the lab is equalized with the storage tanks {32 and 33}, the blow-down phase can be continued, with the pressurized natural-gas supply accumulator {23} expanded into the recovery tanks {32 and 33}. Note that for some operations, it may not be necessary to recover the volume of natural gas in the source accumulator {23}. For instance, if testing will continue after performing necessary service to the natural gas delivery manifold in the lab, the supply accumulator {23} is safe and practical for pressurized natural gas storage. If it is desired to also expand the source accumulator {23} into the natural gas storage tanks {32 and 33}, then the source accumulator manual isolation valve {25} is opened.

As a conservative estimate of the maximum pressure in the natural gas storage tanks after a recovery operation, the full capacity of the source accumulator {23} is included in the calculations [17]. In the above phase of the recovery operation where high pressure natural gas at up to 650 bar-g (9425 psig) is expanded to the recovery system with a maximum operating pressure of 39 bar-g (565 psig), it is important that the recovery system is pressure protected. As a worst-case scenario, the low-pressure compressor system {84} and the high-pressure compressor system {56} can be

isolated from the recovery system by closing isolation valves {26, 36 and 38}. When thus isolated, high-pressure natural gas expanded to the recovery system can only flow into the recovery tanks {32 and 33}. The lowest pressure rated component in this isolated system is the low-pressure pump outlet {92}, which is rated at 70 bar-g (1000 psig) and is therefore assigned as the maximum allowable working pressure of the storage tank system.

As described earlier, a pressure relief valve {28} set to 43 bar-g (620 psig) protects this system from over-pressure. Calculations [17] show that the pressure relief valve {28} cannot accommodate unrestricted flow from the high pressure accumulated volumes passing through isolation valve {37}, so a restrictive flow orifice {39} is necessary in the blow-down line. The restrictive flow orifice {39} ensures that the inlet pressure on pressure relief valve {28} does not exceed the maximum allowable working pressure of 70 bar-g (1000 psig) for this part of the system, and pressure relief valve {28} can properly vent any excess pressure in the event of operator error, such as neglecting to open the recovery tank valves {34 and 35}. There is no commercial restrictive flow orifice available that is rated for 650 bar (9425 psig), so a section of high pressure 1/8-inch tubing with a 0.020-inch inner diameter and a length of 2 inches is employed to act as a restrictive flow orifice {39}. Choked-flow calculations [17] indicate that a 0.020-inch orifice will permit a maximum air-standard flow of ~39 scfm with an upstream pressure of 650 bar-g (9425 psig). If the storage tanks were closed and the blow-down flow through the restrictive flow orifice {39} of 39 scfm were dead-headed into the low-pressure part of the recovery system, then pressure relief valve {28} would open at 620 psig with a resulting inlet pressure of 720 psig [17], which is a safe value for this system (below the 1000 psig maximum allowable working pressure).

After the expansion of the accumulator volumes into the storage tanks {32 and 33} and pressure equalization, the equalized pressure of the natural gas that is distributed among the accumulator volumes, the source cylinder and the plumbing can be as much as 31 bar-g (437 psig) [17]. To transfer as much of this residual natural gas as possible to the storage tanks {32 and 33}, the low-pressure compressor system {84} is used. The low-pressure compressor system {84} has a maximum inlet pressure of 80% of the building compressed air pressure. At a nominal building compressed air pressure of 6 bar-g (90 psig), the maximum inlet pressure is roughly 4.8 bar-g (70 psig). The maximum output pressure of the low-pressure compressor with 6 bar-g (90 psig) compressed air is 43 bar-g (1000 psig) [20]. It is capable of pumping down to as low as 1 bar-a (14.5 psia).

The designed natural gas inlet for the low-pressure compressor is reduced to a pressure of 70 psig by a regulator {53} that is connected to the low-pressure part of the recovery system by an isolation valve {38}. Depending on valve configurations, it is also possible for the output side of the pump to be connected to low-pressure side of the recovery system through another isolation valve {36}. Both of these entry points are protected from over-pressure. If the inlet isolation valve {38} were opened while the high-pressure line is fully energized to 650 bar-g (9425 psig), then the regulator {53} is protected with the restrictive flow orifice {39} matched [17] to the pressure relief valve {14} set at 620 psig. As described in the previous paragraph, the

highest inlet pressure produced in this scenario is ~720 psig. The inlet regulator {53} has a maximum inlet pressure of 3,000 psig, so the restrictive flow orifice {39} and pressure relief valve {14} provide sufficient pressure protection.

On the low-pressure compressor outlet side {92} outlet side, if the outlet isolation valve {36} were opened to expose the outlet side of the low-pressure compressor system {84} while the high-pressure line is fully energized to 650 bar-g (9425 psig), the previous paragraph and calculations [17] show that pressure relief valve {89} in conjunction with the restrictive flow orifice {39} yield a maximum back pressure of 50 bar-g (720 psig). This is sufficient to protect the low-pressure compressor {92} outlet line, which has a pressure rating of 70 bar-g (1000 psig).

On the inlet side of the low-pressure compressor {92}, the weakest component is the low-pressure pilot switch {88}, which is rated to 17 bar-g (250 psig) and thus defines the maximum allowable working pressure of the inlet side of the low-pressure compressor {92}. As described above, the highest pressure on the inlet side of the low-pressure compressor regulator {53} is 70 bar-g (720 psig) with a maximum flow of 39 scfm through the restrictive flow orifice {39}. If the regulator {53} were to fail with this worst-case 70 bar-g (720 psig) inlet pressure, the air-standard flow rate through the regulator {53} would be 20 scfm air [17]. The inlet to the low-pressure compressor {92} is protected by a pressure relief valve {86} set to 6.3 bar-g (92 psig), which will yield a back pressure of 12 bar-g (170 psig) at 20 scfm air. This is below the 250 psig maximum allowable working pressure of the inlet side of the low-pressure compressor {92}.

For the pumping operation to transfer expanded natural gas from the high-pressure system to the storage tanks {32 and 33}, the high-pressure system isolation valve {37} must be closed, and the inlet isolation valve {38} must be opened. The low-pressure pump {92} inlet regulator {53} should be set to 3.4 bar-g (50 psig), which provides sufficient margin below the maximum operational inlet pressure of 4.8 bar-g (70 psig). The low-pressure compressor {92} may then be engaged by opening the compressed air valve {94}. Once the pump starts, the output line dial indicator pressure gauge {91} should show rising pressure if the pump is working properly. As the outlet approaches the equalization pressure of 31 bar-g, then the valve {36} may be opened and the pumping continues until the high-pressure components are pumped down to as low as ~1 bar-a, at which point the natural gas is considered to be fully recovered. The pump is turned off by closing valves {94, 36, and 38}.

After pumping is complete, residual pressure in the inlet and outlet lines to the low-pressure compressor assembly {84} can be relieved through the vent valves {87 and 90}. The pressure in the storage tanks {32 and 33} after the end of pumping depends on the amount of natural gas stored. The largest amount of stored natural gas occurs if the storage tanks {32 and 33} have already been filled to 10 bar-g (145 psig) and all of the accumulators in both the supply and delivery systems and high pressure lines are fully charged, and natural gas in the source cylinder {1}at 10 bar-g (145 psig) is also transferred into the storage tanks {32 and 33}. The source cylinder {1} is included because it may be necessary to recover the remaining natural gas in the source cylinder {1} once the pressure in the source cylinder {1} is depleted to the minimum

high-pressure compressor {60} inlet pressure of ~7 bar-g (100 psig), such that it is too low to further supply the high-pressure compressor {60}. Hence, this natural gas is also included in the maximum storage tank pressure calculations [17]. The resulting pressure in the storage tanks is 35 bar-g (507 psig).

After the storage tanks {32 and 33} are charged with natural gas, they can provide source natural gas to the high-pressure pump assembly {56} to charge the high-pressure supply system. To use the storage tanks {32 and 33} as the natural gas supply, the recovery system output valve {26} must be open. Similar to the source natural gas regulator {8}, the recovery regulator {52} should be set to 31 bar-g (450 psig). Then, the high-pressure compressor operation can proceed. The high-pressure compressor {60} will pump out the natural gas from the storage tanks until the regulated pressure drops below the minimum suction pressure of 7 bar-g (100 psig). Then, the recovery system outlet valve {26} may be closed and the natural gas supply system valve {13} opened so that the compression continues, using the source cylinder {1}.

Finally, in addition to compressing the natural gas source and delivery system contents into the storage cylinders {32 and 33}, the contents of the storage cylinders may also be pumped out into auxiliary tanks through the external output valve {45}. This feature is for the case when a different natural gas mixture is required for testing and the existing natural gas mixture needs to be saved for later use. For such an operation, the auxiliary tanks must equal ~78 L or greater [17] using the maximum operating pressure of 38 bar-g (550 psig) on the outlet side of the low-pressure compressor {84}.

To transfer the natural gas mixture to an auxiliary tank, the auxiliary tanks need to be connected to the external output valve {45} with a flex hose (similar to {5}). The low-pressure compressor {92} output isolation valve {36} and the high-pressure system isolation valve {40} may then be closed. Two other high-pressure isolation valves {37 and 38} then can natural gas to flow out of the storage tanks {32 and 33} and into the inlet regulator {53} of the low-pressure compressor assembly {84}. The pumping operation can then commence, as already described above.

2.1.4. Rough Vacuum System for Pump Down

The portable vacuum system {74} may be connected to the manifold during initial installation, natural gas cylinder exchanges, storage tank evacuation, and maintenance routines. The portable vacuum system [21] can easily be connected onto various ports on the systems when needed. It has direct venting of pressure greater than 1 psig before the pump is engaged to the system. The pump is not to be connected to charged natural gas circuits with pressures greater than 1 psig. This is a manual system and start-up of the vacuum sequence requires that the procedure is manned until the evacuation process has been initiated [21]. Once any positive pressure has been vented or otherwise pumped out of the circuit using the low-pressure compressor assembly {84}, the isolation valves {48 and 75} can be opened and pumping can commence. This unit is not connected during normal operations.

2.2. Natural Gas Fuel Delivery System

The natural gas fuel delivery system, shown in Figure 2, is divided into three separate legs based on the pressure requirements of multiple fuel-injection systems for the engine: 10 bar-g for intake manifold fumigation of natural gas; 100 bar-g for direct injection of natural gas during the intake and/or early compression strokes; and 600 bar-g for high-pressure direct injection of natural gas for mixing-controlled diesel-like combustion. All of the legs may be active simultaneously for a given experiment such that the combined fuel delivery is the sum of the individual contributions from the active legs. The lower-left corner of the schematic in Figure 2 also shows an acetone fuel-tracer vaporizer system [23] that can be installed onto the 10 bar delivery leg for fuel-tracer diagnostics. The acetone fuel-tracer vaporizer system is for fuel-tracer experiments under non-combusting conditions (no oxygen in the engine intake stream). This acetone fuel-tracer vaporizer system is described in Section 2.3.

The functionality and safety considerations common to all three legs is described in the remainder of this section, and each leg is described individually in the subsections to follow. Key components from the schematic in Figure 2 are identified within curly brackets. See [22] for a full listing of all components.

The natural gas fuel delivery system is constructed with both manual and automatic controls. The primary control system is panel mounted, push-button control with safety interlocks. The pressure system, control system, and engine integration are all precisely represented in a set of schematics [22]. For each leg, the fuel injection pressure is set manually using individual regulators {58, 26, 35} for each leg. On each of the legs, both manual pressure gauges {44, 41, 88} and pressure transducers {45, 27, 36} connected to digital read-outs on the control panel provide feedback to the operator for manually adjusting the pressure regulators to the desired injection pressures for each leg.

The regulated delivery manifold for the three legs of the natural gas fuel delivery system is physically located in the northwest corner of laboratory 165 in building 906 of the California site. The primary control system is located at the engine control center and computer table between the engine in the center of the lab and the regulator manifold on the north wall. The delivery manifold receives up to 650 bar-g of natural gas from the fuel source system described in Section 2.1. The main source line branches out to the three separate legs of the delivery manifold.

Overall flammable-gas protection inside the lab is accomplished using two room-air flammable gas detectors and automatic isolation valve {43} in Figure 2, which is the same as the isolation valve {43} of the natural gas fuel source system schematic in Figure 1. This 3-way valve {43} is operated by remote push-button operation located in the flammable gas detection control box {44} along the east wall of lab 165. When the valve is activated (panel reads “HP-NG Valve Opened”), the main source line {34.2} is connected to the source manifold accumulator {23} in Figure 1. If either of the two room-air flammable-gas detectors sense natural gas concentrations in the room exceeding 10% of the lower flammability limit, the 3-way valve {43} is automatically deactivated (panel reads “HP-NG Valve Closed”). This results in the 3-way valve {43} connecting the main source line {34.2} to a roof vent through a one-

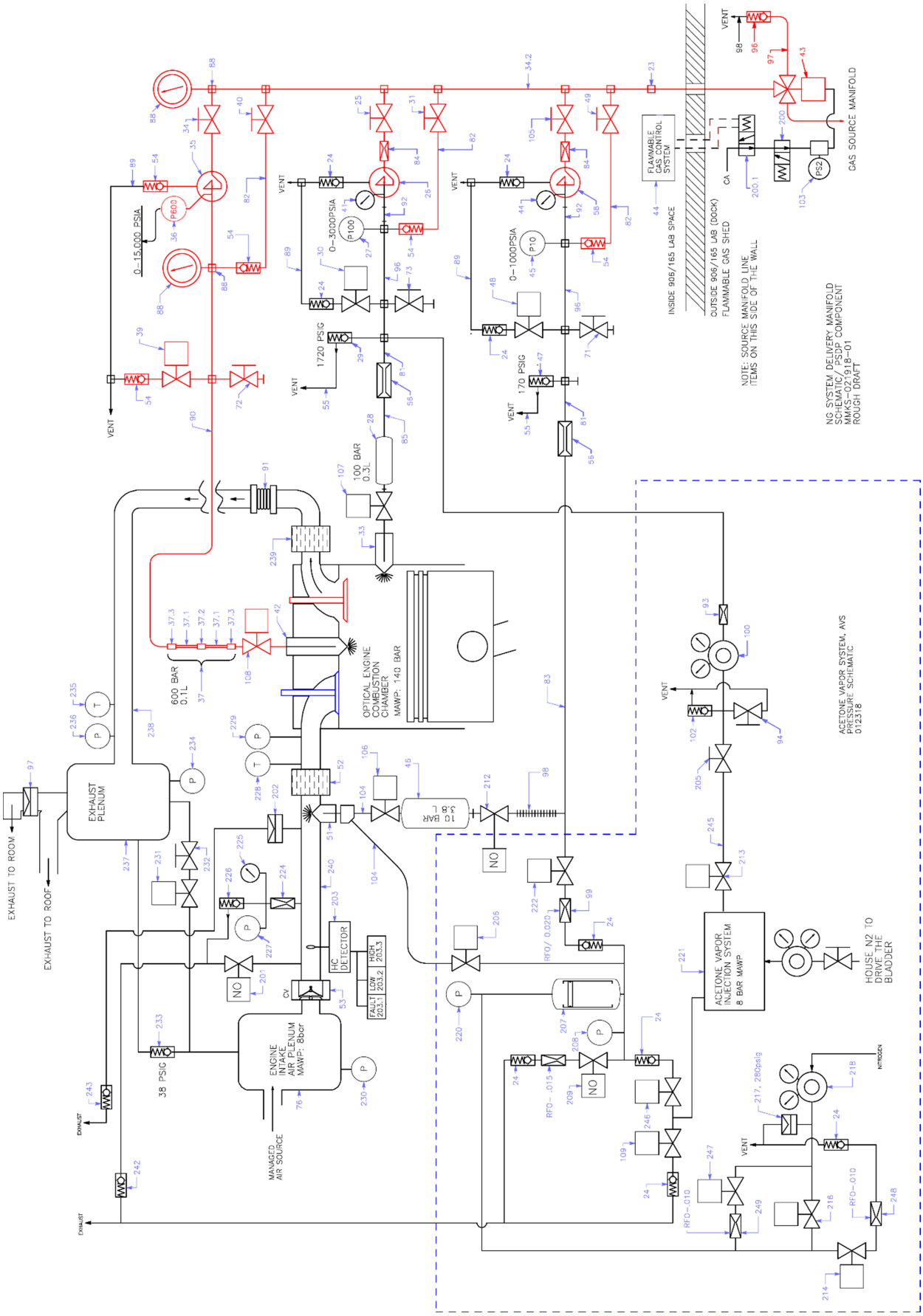

Figure 2. Schematic of natural gas fuel delivery system. See [22] for component list.

way valve {96}. In addition, flammable gas concentrations exceeding 20% of the lower flammability limit will trigger a high-level flammable gas alarm, and a fire response team will automatically be notified that there is a flammable gas detection in the lab.

All three natural gas legs of the delivery manifold (10-bar, 100-bar, and 600-bar) utilize one-way valve loops back to the main source line {34.2} to provide a path for gas in the plumbing of each to return to the main source line {34.2} for automatic venting in the case of a flammable gas detection event. Each branch of the delivery manifold has a pneumatic vent valve that is controlled with the delivery manifold control panel. When the 3-way valve {43} (source manifold) is in the vented (closed) state (including a flammable-gas detection event), the delivery manifold control panel automatically opens each of the three vent valves {48, 30, and 39} on each of the three legs to automatically vent the line plumbing. It also closes all three of the accumulator-to-injector isolation valves {106, 206, 107, and 108}. This action isolates the engine from receiving natural gas and allows the accumulators to be vented properly.

2.2.1. 10-bar Natural Gas Delivery Leg

The 10-bar natural gas delivery line requires special attention for safety considerations, because it uses flammable natural gas injection directly into the intake runner air stream outside the engine rather than into the high-pressure combustion chamber of the engine as the other two higher-pressure legs do. Also, special attention is provided in this subsection both to the exhaust system for failure scenarios that could cause flammable gas mixtures to accumulate in the exhaust plenum and subsequently ignite, and to the intake runner for similar scenarios involving potential ignition of flammable gas mixtures.

In Figure 2, an injector {51} for intake-runner {240} fumigation of natural gas is connected to the 10 bar delivery leg by the isolation valve {106} downstream of the 10-bar accumulator {46}. For typical experiments using this injector {51}, the 10-bar accumulator {46} has sufficient volume to maintain delivery pressure to within 1% during an injection, and is replenished between injections by the 10-bar delivery line {83}.

In addition, an alternate delivery line originates from the acetone fuel-tracer vaporizer system {104} by an isolation valve {206} downstream of a piston accumulator {207}. The accumulator-to-injector isolation valves {106 and 206} are pneumatic valves controlled through the natural gas control panel.

Injecting a flammable gas directly into the airstream of the intake runner, rather than directly into the engine combustion chamber, introduces a high level of rigor with respect to pressure safety. Therefore, much effort is afforded to this system to ensure safe operation.

During engine operation, air and/or nitrogen is heated and pumped into the intake plenum {76} at pressures ranging from 0.4 to 3 bar-a depending on the needs of the experiments. The air plenum {76} is connected to the engine via the intake

runner {240}. The 10-bar injector {51} connects to the intake runner upstream of the engine. The injector pulses natural gas into the intake runner during selected intake cycles of the engine, fumigating the intake stream with natural gas. The natural gas delivered during the injector pulse is emitted into the intake runner by a custom fumigation ring with a series of small holes in a circular pattern. The gas flow created from the engine intake valve opening and subsequent piston motion causes the mix of natural gas and air and/or nitrogen to be swept into the engine combustion chamber.

The 10-bar injector assembly was pressure-tested at Sandia [22] to a value that is 22% above of the 219 psig predicted maximum pressure reached upon catastrophic failure of the regulator {58}. It is appropriately pressure protected by the installation of the pressure relief valve {47} set at 170 psig [22].

There are three passive protection devices installed in the intake runner. First, a flame arrestor {52} is installed in the intake runner {240} between the location of the 10-bar injector {51} and the engine. At some points over the course of an engine combustion experiment, a flammable mixture of natural gas and air typically exists in the intake runner originating due to injection of natural gas by the injector {51} and subsequent mixing with air inside the intake runner before it is swept into the engine during an intake cycle. The flame arrestor is designed to prevent a flame or ignition source from passing from the engine into the intake runner. In the case where the flammable gas mixture is entering the engine combustion chamber and the intake valve is not yet closed, a deflagration will be stopped from going further back than the flame arrestor. In addition, if the injection pulse is premature, causing the flammable gas mixture to accumulate before the intake valve is opened, a flame or ignition source emitted from the engine combustion chamber while the intake vale is open is stopped by the flame arrestor from going back into the intake runner and igniting the mixture in the intake runner.

Second, a large butterfly-type check valve {53} is installed where the intake runner {204} connects to the intake plenum {76} to prevent flammable gas from going backward into the air plenum. If there is positive flow of air coming from the air plenum {76} the check valve will remain open. At times when there is insufficient intake airflow to hold the check valve {53} open, springs in the check valve return it to a closed condition, preventing backflow into the intake plenum {76}. Once the check valve {53} is closed, any increase of gas pressure in the intake runner, for instance due to natural gas injection or resulting from limited deflagration between the flame arrestor {52} and the engine, will stay in the intake runner {204} and not migrate to the air plenum {76}. This passive protection is designed to prevent flammable-gas mixtures from ever entering the intake air plenum.

Third, a 1-inch diameter burst disc {202} with a 45 psig burst pressure at 160 ºC (peak operating temperature for the intake runner) is installed onto the intake runner {204}. If the pressure in the intake runner reaches 45 psig during operation due to a stuck injector {51} or a deflagration between the flame arrestor {52} and the engine, the burst disc {202} will rupture and vent gas to the lab vent system.

In addition to the above passive controls, the intake runner {204} is also equipped with several engineered controls. The first order of engineered control is established

through control of the injector pulse. The pulse is timed to deliver natural gas at appropriate times during the engine cycle when any flammable mixture created by the injection will quickly be swept into the engine combustion chamber, which is designed to withstand pressures generated by combustion.

Second, the 10-bar accumulator {46} supplies a continuous source of natural gas to the injector via isolation valve {106} during combustion experiments, or through isolation valve {206} during non-combusting fuel-tracer diagnostic experiments. These valves are normally closed (spring closed) pneumatic valves. They both required power to be opened, and are hence fail-safe by design. Valve {106} has a feature that requires a power loop to be completed for the valve to receive electrical power. The connector is located on the back panel of the natural gas control panel. The loop will only be completed during engine runs as required. This prevents the injector from being charged with natural gas when the engine is not running.

Third, a hydrocarbon detector {203} is installed into the intake runner near the air plenum {76}. Under normal operating conditions with a positive flow of air out of the intake plenum {76}, no flammable gas should ever exist at the location of the hydrocarbon detector. If the flammable gas is present at this location, the hydrocarbon detector will enter alarm states at two different levels. The low-level alarm indicates on the control panel and turns on am audible alarm to warn the operator that there is a flammable gas detection in the intake runner. If the high-level alarm is detected, the 10-bar accumulator-to-injector isolation valve {106} and the acetone fuel-tracer vaporizer isolation valve {206} are automatically closed, thereby preventing the injector from being supplied with natural gas. Simultaneously, the intake runner pneumatic vent valve {201} automatically vents the intake runner to the roof. These functions will remain latched until cleared by the operator through interface with the natural gas control panel. This engineered feature is designed to act before a flammable mixture is obtained anywhere near the air plenum {76}.

Fourth, a pressure transducer {227} measures the pressure in the intake runner {204}. The signal is sent to the natural gas control panel and into a pressure controller. The relay in the pressure controller is operator-set to an alarm-level pressure above that required for experiments. If an alarm-level pressure is detected, the control panel automatically closes the 10-bar accumulator-to-injector isolation valve {106} and the acetone fuel-tracer vaporizer system isolation valve {206}, and opens the intake runner vent valve {201}. This mitigates further pressure increase from any natural gas that would pass through the injector, and also vents the intake runner {204} through the vent system. These functions will remain latched until cleared by operator through interface with the natural gas control panel.

Even though great effort has been expended in the design of the 10-bar injection system and intake runner system to prevent undesired ignition or deflagration outside the engine, certain unanticipated failure scenarios might indeed lead to ignition of flammable mixtures outside the engine. Hence, mitigation of such unlikely scenarios is included in the design of the systems, as described below.

Considering first the scenario of an unanticipated ignition source and subsequent deflagration in the exhaust plenum, it is possible that under some engine operating

conditions, unburned natural gas may pass through the engine and accumulate in the exhaust plenum {237} after being mixed with air. A flame arrestor {239} is placed between the engine and the exhaust plenum {237} to prevent ignition sources associated with combustion inside the engine from reaching any flammable mixture that might accumulate in the exhaust plenum. Even with this precaution to prevent ignition, pressure relief is implemented on the exhaust plenum as an additional safety measure. A 3-inch burst disk {97} is mounted as close as possible to the exhaust plenum {237} to relieve any excess pressure that might be generated by some unanticipated ignition source and subsequent deflagration. Standard engineering approaches exist for design and sizing of venting for pressure vessels like the exhaust plenum [24, 25, 26]. Appendix A includes detailed calculations of the peak pressure that would be reached inside the vented exhaust plenum in such a scenario. The calculations show that the 3-inch burst disk {97} is sufficient to protect the exhaust plenum {237} from damage.

The worst-case scenario for the intake runner is that it is fully filled with a stoichiometric mixture of natural gas and air initially at 3 bar-a pressure, and that the mixture is ignited by some unanticipated ignition source. Calculations provided in Appendix B show that for the short ~2 m length of the intake runner, significant increase in the turbulent flame speed and/or a transition to detonation are unlikely, and the 1-inch burst disk {202} should be sufficient to protect all intake manifold components from damage. However, due to a lack of established standards or reference data at similar conditions, significant uncertainties exist in the venting requirements at the high pressure (3 bar-a) and high temperature (160 ºC) conditions required by the experiments for the gases inside the intake runner. Given these uncertainties, it is imperative to use all available means to avoid an ignition event, which is the reason for the degree or rigor in the passive and active pressure and ignition controls described above.

2.2.2. 100-bar Natural Gas Delivery Leg

The fuel delivery system up to the injector for the 100-bar injection system parallels that of the 10-bar natural gas delivery leg of Subsection 2.2.1. In Figure 2, the 100-bar injector {33} for direct injection of natural gas through a side-port in the cylinder wall of the engine is connected to the 100-bar delivery leg by the isolation valve {107} downstream of the 100-bar accumulator {28}. For typical experiments using this injector {33}, the 100-bar accumulator {28} has sufficient volume to maintain delivery pressure within 1% during an injection, and is replenished between injections by the 100-bar delivery line {85}.

The 100-bar natural gas delivery leg also includes a spur to supply the acetone fuel-tracer vaporizer system with a carrier flow of natural gas at sufficiently high pressure for down-regulation to the necessary internal pressure and with sufficient flow rate. The 100-bar delivery leg was also chosen for this spur because the 10-bar leg is dedicated to filling the accumulator piston {207} when the acetone fuel-tracer vaporizer system is used. This carrier gas supply spur includes a pressure regulator {100} with an appropriately sized [22] restrictive flow orifice {93} and

pressure relief valve {102} for pressure protected delivery of natural gas to the acetone vapor system at a nominal pressure of 20 bar-g.

2.2.1. 600-bar Natural Gas Delivery Leg

The fuel delivery system up to the injector for the 600-bar injection system also parallels that of the 10-bar natural gas delivery leg of Subsection 2.2.1. In Figure 2, the 600-bar injector {42} for direct injection of natural gas through a centrally mounted location in the cylinder head is connected to the 600-bar delivery leg by the isolation valve {108} downstream of the 600-bar accumulator series {37}. A single 600-bar accumulator of sufficient volume was not available, so three smaller accumulator units {37.1} of sufficient total volume to maintain delivery pressure within 1% during an injection are connected in series. The accumulator series {37} is replenished between injections by the 600-bar delivery line {90}.

2.3. Acetone Fuel-Tracer Vaporizer System

The purpose of the acetone fuel-tracer vaporizer system shown as a block {221} in Figure 2 is to deliver flow of natural gas seeded with vaporized acetone to the piston accumulator {207} of the 10-bar leg of the natural gas fuel delivery system for fuel-tracer experiments. Although fuel-tracer experiments have not yet been conducted and hence results are not included in this report, the original proposal anticipated a need to

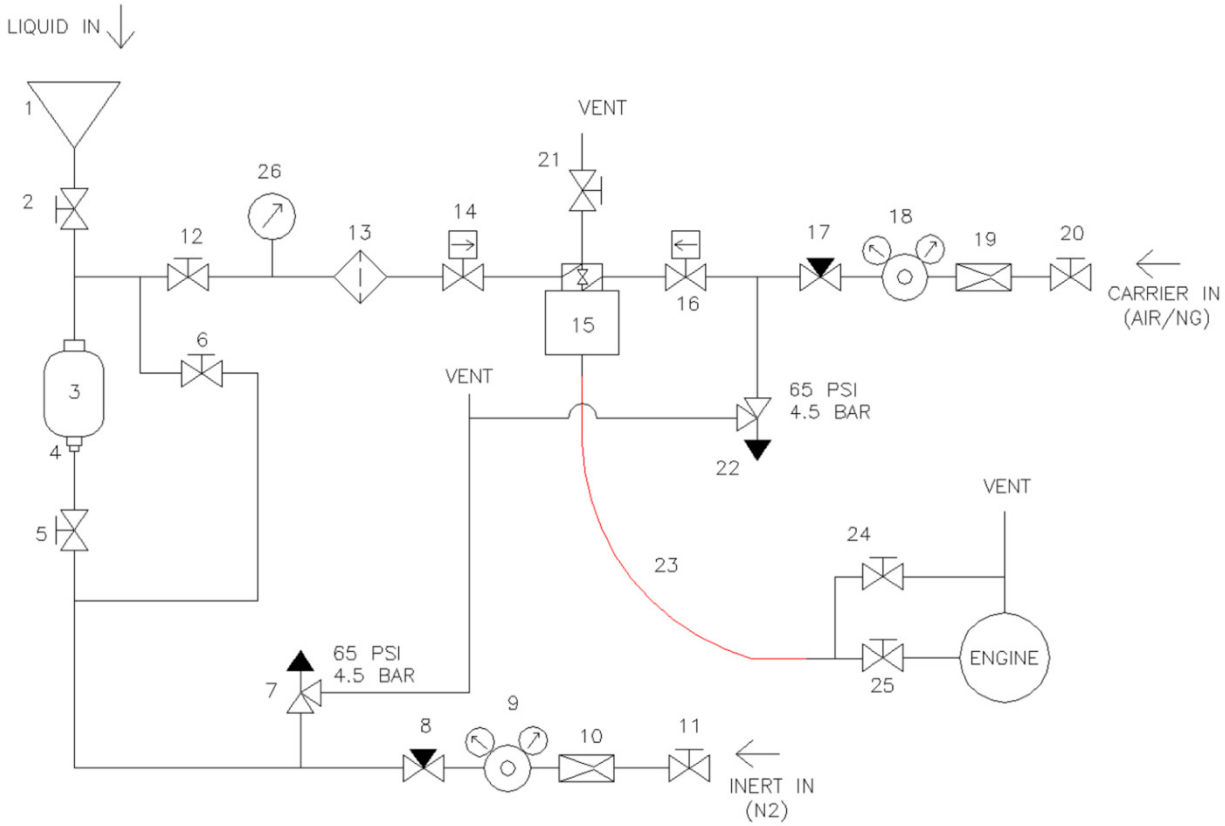

Figure 3. Schematic of acetone fuel-tracer vaporizer system. See [23] for component list.

use fuel-tracer diagnostics to measure the mixing state of the natural gas and air inside the engine, hence the construction of the acetone fuel-tracer vaporizing system as part of this project. The acetone fuel-tracer vaporizer system will be used in experiments for additional work that will follow the conclusion of this project.

A schematic of the acetone fuel-tracer vaporizer system that corresponds to item {221} from Figure 2 is shown in Figure 3. The acetone fuel-tracer vaporizer system is located inside of 906/165 on a custom-made Unistrut cart. The functionality and safety considerations for the acetone fuel-tracer vaporizer system is described in this section.

The heart of the vaporizer system is the evaporator/mixer {15} in Figure 3, which combines natural gas, whose flow is controlled by one flowmeter/controller {16}, with a liquid fuel-tracer, typically acetone, whose flow is controlled by a second flowmeter/controller {14}. The evaporator/mixer {15} vaporizes the inlet acetone flow using an electric heater and mixes it with the natural gas flow before delivering it to the natural gas fuel delivery system of the engine through the heated line {23}.

The evaporator/mixture {15} requires that both the natural gas and liquid acetone flows are provided at an appropriate inlet pressures for metering by the flowmeter/controllers {14 and 16}. For the liquid acetone inlet to flowmeter/controller {14}, the accumulator {3} is partially filled by the user by pouring liquid acetone into the funnel {1}, after which the fill valve {2} may be closed and pressurized nitrogen gas supplied to the other side of the bladder through valve {5} at the required pressure as controlled by a pressure regulator {9}. The nitrogen pressure on the accumulator bladder in turn pressurizes the liquid acetone inlet flow to the flowmeter/controller {14}, which is filtered {13} to remove particles that may interfere with the operation of the flowmeter/controller {14} and/or the evaporator/mixer {15}. The acetone flowmeter/controller {14} is protected from overpressure that could result from a catastrophic failure of the regulator {9} by an appropriately sized [23] restrictive flow orifice {10} and pressure relief valve{7}. An inert gas delivery system supplies compressed nitrogen from the service apron outside the laboratory through valve {11}.

On the natural gas side of the evaporator/mixer {15}, pressure-regulated natural gas from the 100-bar leg of the natural gas fuel delivery leg of Subsection 2.2.2 is delivered through valve {20} and reduced to the necessary pressure for the natural gas flowmeter/controller {16} by a pressure regulator {18}. The natural gas flowmeter/controller {16} is protected from overpressure that could result from a catastrophic failure of the regulator {18} by an appropriately sized [23] restrictive flow orifice {19} and pressure relief valve {22}.

2.4. Optical Heavy-Duty Diesel Engine Retrofit for Natural Gas Fueling

Natural gas combustion processes were measured in a single-cylinder, direct-injection, 4-stroke diesel engine based on a Cummins N-series production engine that was retrofitted for natural-gas fueling for this project. A side-view schematic of the engine is shown in Figure 4, and the specifications of the engine are summarized in Table 1. The original diesel version of this engine has been used in other studies and a

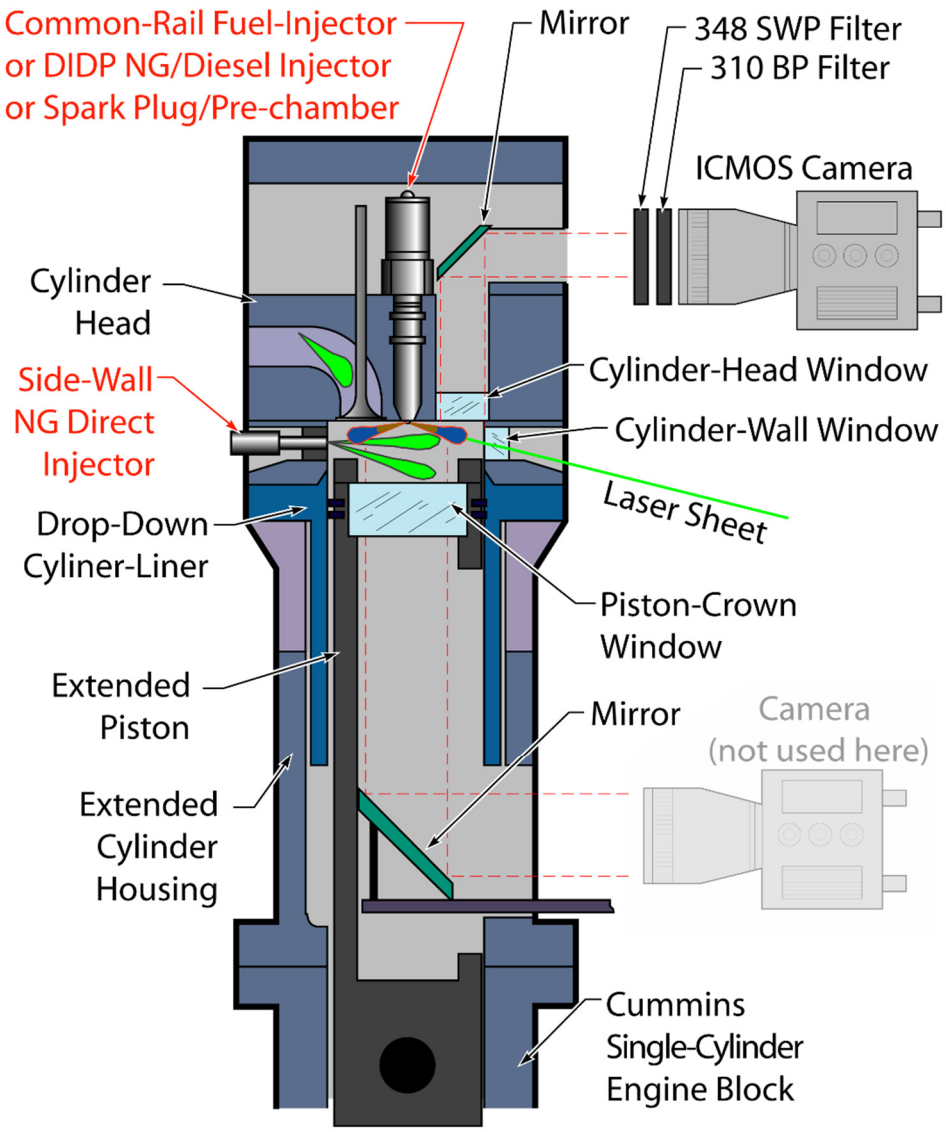

Figure 4. Extended-piston optical heavy-duty diesel engine and squish-region OH* imaging setup. Natural-gas-fueling retrofit-equipment is labeled with red text.

complete description of the engine and its specifications is available elsewhere [27]. A brief description of the engine follows.

The Cummins N-series engine is typical of heavy-duty size-class diesel engines, with a bore of 140 mm and a stroke of 152 mm, yielding a displacement of 2.34 liters per cylinder. These dimensions are retained in the single-cylinder, optically-accessible engine. The intake port geometry of the production cylinder head also is preserved, yielding a quiescent (low swirl) combustion chamber. The optical engine is designed so that the upper cylinder liner separates and drops down from the head without engine disassembly, allowing rapid cleaning of in-cylinder optical surfaces. To provide optical access, the engine is equipped with an extended piston and flat piston-crown window for views from below of the combustion bowl in the piston.

Table 1. Engine and Injector Specifications

Engine base type	Cummins N-14, DI diesel
Number of cylinders	1
Number of intake valves	2
Number of exhaust valves	1*
Combustion chamber	Quiescent, direct injection
Swirl ratio	0.5
Bore × Stroke, cm	13.97 × 15.24
Bowl width, depth, cm	9.78, 1.55
Displacement, liters	2.34
Connecting rod length, cm	30.48
Geometric comp. ratio	11.2:1
Fuel injector type	Modified GM/Bosch LT4 GDI
Needle type	Inward opening
Number of orifices	1
Orifice diameter, mm	1.0

* In this optically accessible diesel engine, one of the two exhaust valves of the production cylinder head was replaced by a window and periscope.

Additionally, a periscope in the cylinder head and a cylinder head window in place of one of the exhaust valves provides a top-down view of combustion in parts of the piston bowl, as well as the "squish" region between the outer piston rim and the cylinder head, and the narrow crevice region between the outer diameter of the piston and the inner diameter of the cylinder wall. It is this top-down view that is utilized in the experimental results presented in this report.

The engine has been retrofit for direct-injection natural gas fueling by adding a modified version of a gasoline direct injector (GDI), model GM LT4, manufactured by Bosch. Specifications for the fuel injector are included in Table 1. This injector was modified to have a single, large hole of 1 mm diameter, and with no sac. The injector is installed in a side-window port in the engine, as shown in Figure 4.

As listed in Table 2, the engine operating conditions in this report use a synthetic natural gas mixture composed primarily of methane (CH_4, 95% by volume), with minor constituents ethane (C_2H_6, 4%) and propane (C_3H_8, 1%). While natural gas is mostly methane, it is the minor components that are critical, because longer-chain hydrocarbons ethane and propane, which are typically present in commercial natural

Table 2. Engine Operating Conditions

Engine speed, RPM	600
Nominal intake temperature, ºC	135
Nominal intake pressure, bar-a	1.3
Start of natural gas injection, CAD	40
Duration of injection, ms (ºCA)	36.6 (132)
Charge-gas lambda [-]	0.91
Laser spark timing, CAD	335
Motor:skip-fire ratio	19:1
Fuel	Synthetic natural gas
CH_4 content, % vol	95.0
C_2H_6 content, % vol	4.0
C_3H_8 content, % vol	1.0
Natural gas supply pressure, bar-a	100

gas, display the low-temperature chemistry [16] that governs knock propensity. Hence, the composition of the natural gas mixture used in the experiments is certified to within ±2% relative. Such certification is expensive, but necessary, because the objective of assessing the fidelity of the chemical kinetics mechanisms of the 0-d model requires that the composition of the fuel in the experiments be specified as precisely as possible given the key role of the minor components in the autoignition chemistry.

For all experiments included here, the engine is operated with the modified GDI on the 100-bar leg of the natural gas fuel delivery system. Although not utilized in this report, the engine may also be fueled with natural gas using the intake runner fumigation injector on the 10-bar leg of the natural gas fuel delivery system, which is described in Section 2.2.1. Additionally, while not yet implemented, the engine and natural gas fuel delivery system described in Section 2.2 has the capability for a future addition of a centrally mounted high-pressure direct-injection (HPDI) fuel injector in place of the stock diesel fuel injector. The HPDI would provide diesel-like injection of natural gas on the 600-bar leg of the natural gas fuel delivery system.

2.5. Optical Diagnostics and Engine Operating Conditions

Figure 5 shows a schematic of a top-down view of the engine combustion chamber, as well as the field of view through the periscope and cylinder-head window (top-right). The piston bowl is in the center of the chamber, and is represented by the light blue disk in the center of the schematic. The squish region is outside the bowl, and is represented by the gray ring outside the piston bowl. The single-hole side-mounted

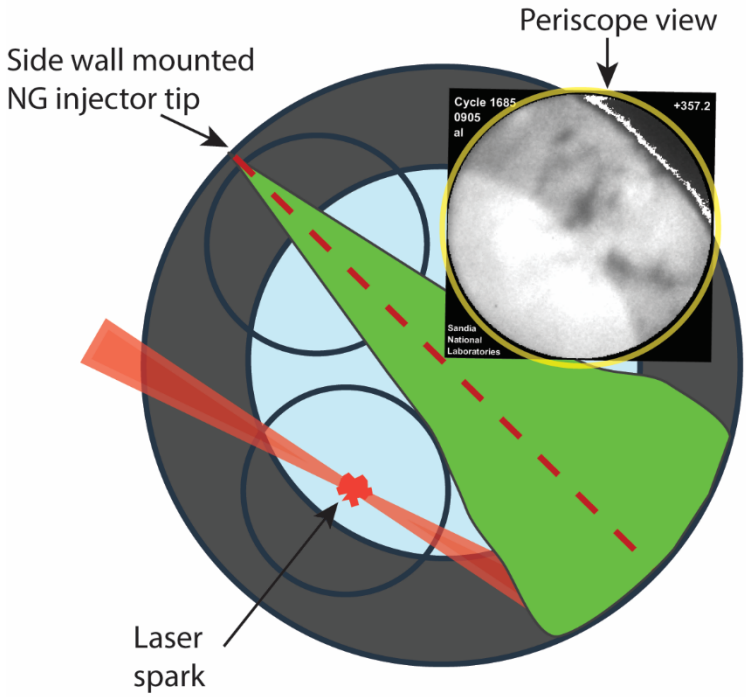

Figure 5. Schematic showing a top-down view of the engine combustion chamber, with the piston bowl (light blue) in the center and the squish region (gray) outside the bowl. The single-hole side-mounted natural gas injector creates a diagonal jet of natural gas during the intake stroke, represented by the green region. The field of view through the periscope and cylinder-head window is in the upper-right of the schematic, where an example image of OH* chemiluminescence is overlaid. A laser beam is focused to a small spot to create a laser spark directly opposite of the field of view to ignite the mixture of natural gas and air in the late compression stroke.

natural gas injector creates a diagonal jet of natural gas during the intake stroke, represented by the green region. At 100-bar injection pressure, the natural gas jet reaches sonic velocities in/at the injector tip (top-left in Figure 5) and subsequently penetrates across the entire chamber at high velocity into the relatively low-pressure intake charge during the induction stroke and creates a tumble motion as it is turned downward at the far side of the chamber (bottom-right), which will aid mixing of the natural gas with air prior to ignition by a laser spark. The field of view through the periscope and cylinder-head window is in the upper-right of the schematic, where an example image of OH* chemiluminescence is overlaid.

While production spark-ignition engines typically use a high voltage spark plug to generate a spark to initiate combustion, these experiments use a focused laser beam. The laser-spark approach as implemented for these experiments has the advantage of a configurable spark location. That is, the beam can be directed through one of multiple side windows shown in Figure 4 over a range of incidence angles to sweep across the width and height of the chamber, and with a range of focal distances to sweep across the depth of the chamber. This allows the spark to be placed in locations that would be

impossible with a conventional spark plug due to geometric constraints (e.g., directly below an intake or exhaust valve). Here, a 10-ns pulsed 532-nm laser beam with a pulse energy of 160 mJ is focused to a small spot to create a laser spark directly opposite of the field of view, about 15 mm below the firedeck and about 35 mm offset from the cylinder axis (bottom-left in Figure 5). This position of the laser spark is intentionally chosen such that the last fuel to burn (the "end-gas"), which is where knock occurs, is aligned with the view through the cylinder-head window (farthest distance from the spark). The laser-spark timing is set to 335 crank-angle degrees (CAD) to ignite the mixture of natural gas and air in the late compression stroke.

High-temperature reactions during combustion generate excited-state hydroxyl radicals (OH*), and the resulting luminous emission resulting from these chemical reactions (chemiluminescence), is a good indicator of high-temperature reaction zones, including both deflagration and knock [28]. Images of OH* chemiluminescence, such as the example image overlaid in the upper-right corner of Figure 5, are acquired by a high-speed Phantom v7.1 complementary metal oxide semiconductor (CMOS) camera, coupled to a high-speed intensifier with a UV-sensitive S-20 photocathode, and equipped with a 50-mm f/4 UV lens. Two filters in front of the lens, a 310 nm center wavelength 10-nm wide bandpass filter and a 348-nm short-wave-pass filter, isolate the OH* chemiluminescence from other emission sources. The camera and intensifier are triggered in bursts of 5 pulses at 19,000 pulses per second, with each pulse burst triggered at one-degree intervals on the engine shaft encoder. This method of camera and intensifier triggering is designed to provide the fastest possible frame rates to capture the rapid onset and development of engine knock while keeping the images synchronized with the engine crankshaft. The camera exposure and intensifier gate duration are set to 49 microseconds, and the windowed camera resolution is 320 (horizontal) by 312 (vertical) pixels.

As listed in Table 2, the intake temperature (135 ºC), intake pressure (1.3 bar-a), charge-gas lambda (0.91), laser-spark timing (335 CAD), and engine speed (600 rotations per minute, RPM) were selected to maximize the knocking propensity of the engine within the range of conditions achievable. For these conditions, light to moderate knocking occurs in approximately 80% of the fired cycles. To minimize thermal loading on the in-cylinder surfaces, the engine is skip-fired, with one fired cycle with natural gas injection and laser spark followed by 19 motored cycles with no natural gas injection or laser spark. This wide 19-cycle interval was also found to be necessary to allow the engine dynamometer, which controls the speed of the engine, to return the engine to the 600 RPM setpoint before it was accelerated again by the next fired cycle.

2.6. Zero-Dimensional (0-d) Modeling

Although detailed models are typically computationally cost-prohibitive in a full engine model, this project is strategically designed to use a zero-dimensional (0-d) formulation that enables full detailed chemical kinetics. The 0-d model is implemented using the closed reactor model of the Chemkin suite for modeling and simulation of gas-phase and surface chemistry [29]. The model was constrained to have zero exchange of heat with its surroundings (adiabatic) and was constrained by the

measured cylinder pressure trajectory from the experiments. In this way, the model simulated a portion of the in-cylinder as-yet unburned fuel-air charge (end-gas) that experiences zero heat transfer and is compressed by the movement of the piston and/or the expansion of hot gases in the deflagration zone initiated by the spark. Such calculations are most representative of portions of the charge that are outside the boundary layers near the walls, and thus experience low heat-transfer losses. It is in these regions that the hottest mixtures are expected, and hence should experience the earliest onset of knock. In other words, although the in-cylinder is highly non-uniform during the initial flame propagation that precedes knock, the model only needs to simulate the characteristic local region that first transitions to autoignition (knock), which allows the adiabatic, pressure-constrained 0-d treatment. This formulation also does not account for heat or mass transfer from the deflagration zone, and hence also essentially represents regions not are not in close proximity to the edge of the deflagration region. The implications of this aspect of the model assumptions are discussed further in Chapter 3, when the results of the engine experiments and model simulations are presented.

Four different chemical-kinetics mechanisms for natural gas combustion are evaluated in the model. The most recent is an as-yet unpublished C_0-C_3 detailed chemical mechanism developed by Miller in 2018 [30], with 171 species and 1143 reactions. This model is of particular interest because (a) it is not tuned to any particular bulk experimental dataset, (b) it utilizes rigorous pressure dependence valid up to 100 bar for all pressure-dependent reactions, and (c) it captures some crucial recent developments in theoretical chemical kinetics, such as the formation of vibrationally hot radicals. A second mechanism that is evaluated is the AramcoMech2.0 C_0-C_4 detailed chemical kinetic mechanism developed by NUI Galway in 2017 [31]. This mechanism has 493 species and 2716 reactions, many of which are not required for knock prediction, but are useful for coupling to larger mechanisms with longer hydrocarbon chains, e.g. [32]. To also assess the performance of a state-of-the-art reduced mechanism, we selected the 2016 CSU141 reduced mechanism from Colorado State University [33], which has 141 species and 709 reactions. Finally, although not considered to be state-of-the-art, we also evaluate the GRIMech30 mechanism developed by the Gas Research Institute and maintained by UC Berkeley [34] because of its historical significance. This 53-species, 325-reaction mechanism is no longer under development, and was last updated near the year 2000.

3. RESULTS OF EXPERIMENTS AND MODELING

The scientific results of this project include both experimental measurements and 0-d model predictions using various chemical-kinetic mechanisms. The experimental data include the timing of the onset of knock as indicated by cylinder pressure measurements, correlated with OH* chemiluminescence images of knocking combustion characterized according to the spatial location of the onset of knock. The modeling results include a predictions of the timing of the onset of knock as indicated by a temperature threshold, which are compared to the measured timing of the knock onset. Key results for both the experimental measurements and the model predictions are presented in the following two sections

3.1. Experimental Results

Presented in this section are image sequences of high-speed OH* chemiluminescence as viewed through the cylinder head window shown in Figure 5. For each presented image, the timing of each frame in CAD is plotted on the upper right corner, and individual images in a figure are identified for discussion by letter in the lower-right corner. The raw OH* chemiluminescence intensity is rendered in grayscale, with white representing the strongest OH* chemiluminescence emission. The images are also post-processed to indicate the difference in the OH* chemiluminescence distribution for one image relative to the preceding image. The images are binarized using a threshold of 25% of full scale as an indicator of the presence of OH* chemiluminescence from high-temperature combustion reactions, and the difference of sequential binarized images is false colored red. In this way, the red color in any particular image shows a visual indication of where OH* chemiluminescence exceeding the threshold appears in that image but did not appear in the previous image.

Figure 6 shows a sequence of OH* chemiluminescence images, post-processed as described above, for a cycle where the onset of knock occurs in the squish region (see Figure 5 for reference regarding the location of the squish region within the image). The leftmost two images (a and b) in the top row, acquired at 358.6 and 359.6 CAD, precede knock and are dominated by flame propagation. The thin red-colored ribbon on the periphery of the bright region of OH* chemiluminescence indicates that the deflagration propagating through the in-cylinder charge of air and natural gas advances a relatively small amount during the 52.6 ms interval between individual frames acquired at 19,000 frames per second. Indeed, the two images (a and b), acquired a full crank angle degree (0.278 ms) apart, appear nearly identical.

The third image from the left (c), however, acquired at 359.8 CAD, only 52.6 ms later than the second (b) image, features a sizeable bulb of red largely isolated from the previous OH* chemiluminescence region. The large size of the red bulb in this image relative to the thin ribbon in the previous two images, which is characteristic of all images prior to 359.8 CAD, is indicative of the onset of knocking. The next image in the sequence (d) features an even larger red region as the knocking combustion rapidly proceeds into more of the unburned end-gas mixture.

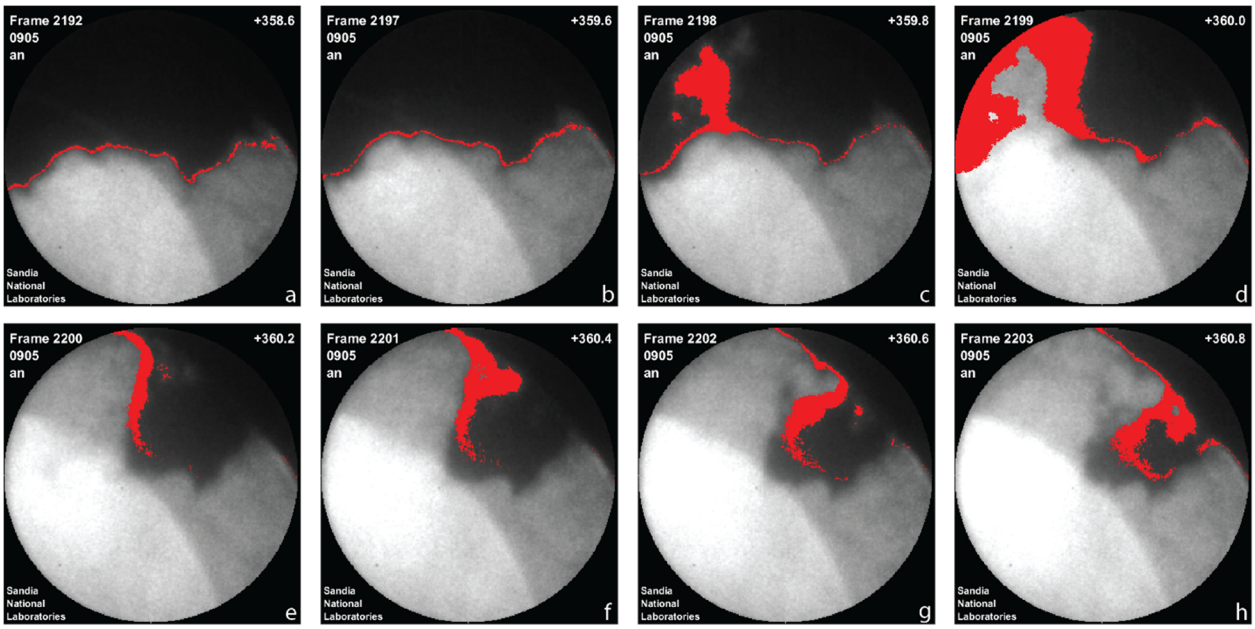

Figure 6. Sequence of grayscale OH* chemiluminescence images for a cycle where onset of knock occurs in the squish region, but is spatially isolated from the propagating deflagration that precedes knock. The image timing in CAD is indicated in the top right of each image. The regions false-colored red indicate the change in OH* chemiluminescence intensity that exceeds 25% of full scale of the current image compared to the previous image.

Thereafter, the knocking combustion proceeds somewhat more slowly through the unburned end-gas in the next four images (e-g), though still considerably faster than the deflagration that preceded knock (images a and b). As the knock proceeds through these later images, the thin ribbon at the edge of the deflagration no longer appears in the images, indicating that the spatial extent of the deflagration did not significantly change. This is likely due to the expansion of the burned gases in the knocking region displacing the end-gas and deflagration region in a direction away from the knocking location. Indeed, even the first knocking image (c) shows a perceivable thinning of the red deflagration ribbon, even if it does not disappear entirely.

The sudden increase in the size of the red region that indicates the onset of knock is also correlated with the rapid rise in cylinder pressure associated with knocking combustion. The plot in the top-left corner of Figure 7 shows the measured cylinder pressure, measured apparent heat-release rate (AHRR), and simulated heat release rate for this cycle, along with similar plots for five other cycles of different knock onset characterizations that will be discussed below.

In the top-left plot, the cylinder pressure (black) rises rapidly near 360 CAD, approximately coincident with the appearance of the red bulb in image (c) of Figure 6. The AHRR curve (red), shows a gradual rise and decline prior to 360 CAD due to the deflagration that precedes the onset of knock. At 359 CAD, the AHRR begins to rapidly increase in a narrow spike indicative of knocking combustion, peaking at 360.5 CAD. Comparing to Figure 6, the largest frame-to-frame increase in the area of

OH* chemiluminescence (largest red area) occurs at 360.0 CAD, which is between the initial rise and the peak in the AHRR.

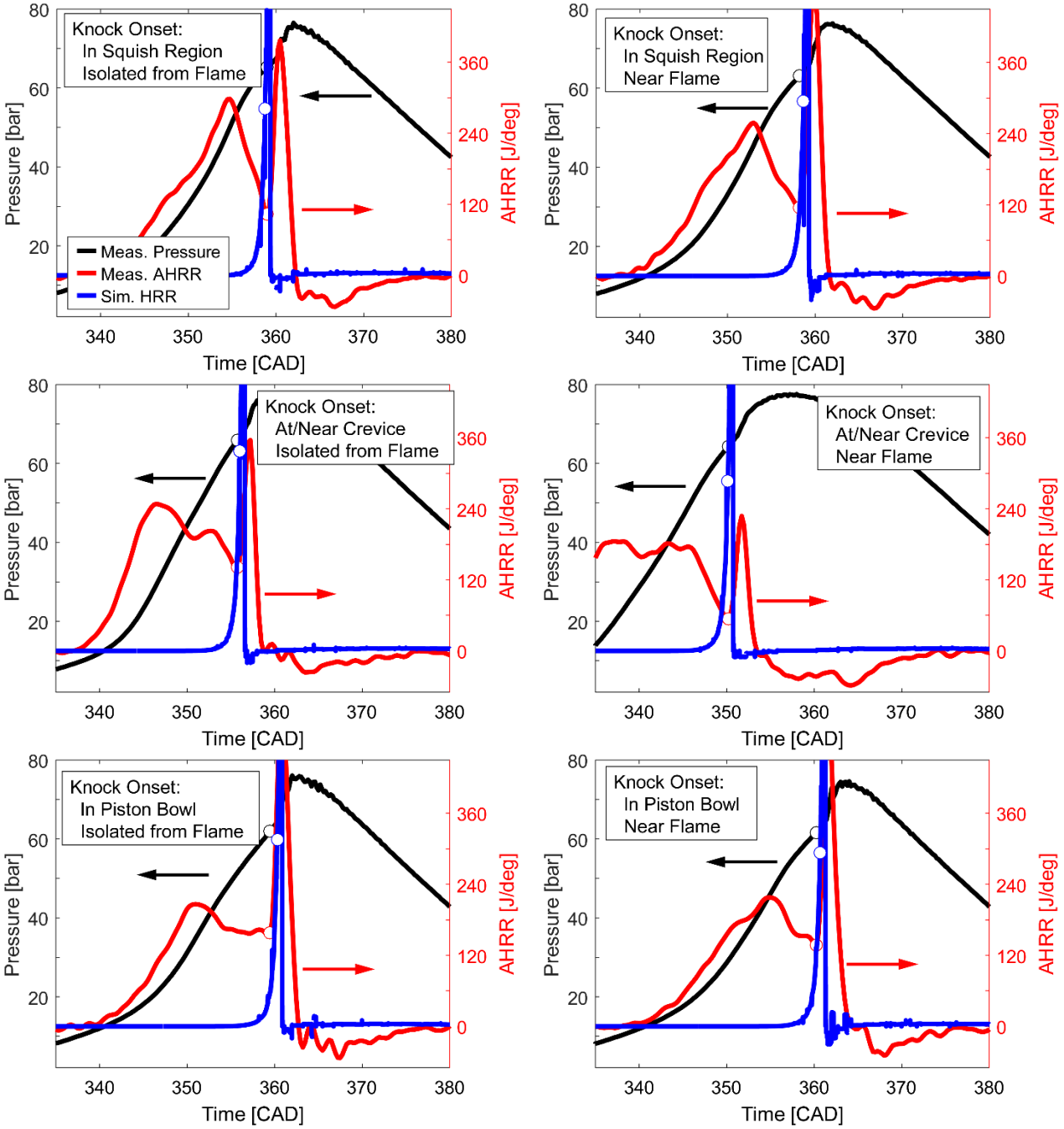

Figure 7. Measured cylinder pressure (black), measured AHRR (red) and simulated heat release rate (blue) using the 2018 Miller chemical kinetic mechanism [30] for six characterizations of the onset of knock, as labeled for each plot. The symbols indicate the knock onset timing indicated by measurements or simulation on their respective curves.

Figure 8 shows a similar sequence of images from a different cycle where the onset of knock again occurs in the squish region, but this time in much closer proximity to the flame. Unlike the image sequence in Figure 6, in the first three images of this sequence (a-c), the thickness of the ribbon at the leading edge of the deflagration region increases, indicating and acceleration of the combustion zone. In the next three images (d-f), the extent of the red region in each image grows rapidly, but still in a roughly thick ribbon shape rather than the broader regions observed during knocking in Figure 6. Although this image sequence, with onset of knock in the squish region but much nearer the flame, shows a much different progression of OH* chemiluminescence from image to image than for the sequence in Figure 6 where the knock onset is more spatially isolated from the flame, this visual indication of the transition to knocking is still well correlated to the rise in cylinder pressure associated with knocking combustion (see top-right plot in Figure 7).

Figure 9 shows an example sequence of images with knock onset near the crevice but isolated from the deflagration zone. The first four images (a-d) show the progression of deflagration preceding knock, and akin to the thinning of the red deflagration ribbon near the onset of knock in Figure 6, the deflagration in these images also progressively thins, even before the OH* chemiluminescence in the regions about to transition to knock have crossed the threshold for being false-colored red. This thinning, indicative of a less rapid growth of the region of OH* in the deflagration zone, could be explained by gas expansion due to heat release in the regions about to transition to knock but that do not yet display strong OH* chemiluminescence. Indeed, in the next image in the sequence (e), the deflagration ribbon disappears (within blue dashed-line ellipse in Figure 9) opposite the location near the crevice that transitions to the red coloring indicative of strong OH* chemiluminescence associated with the

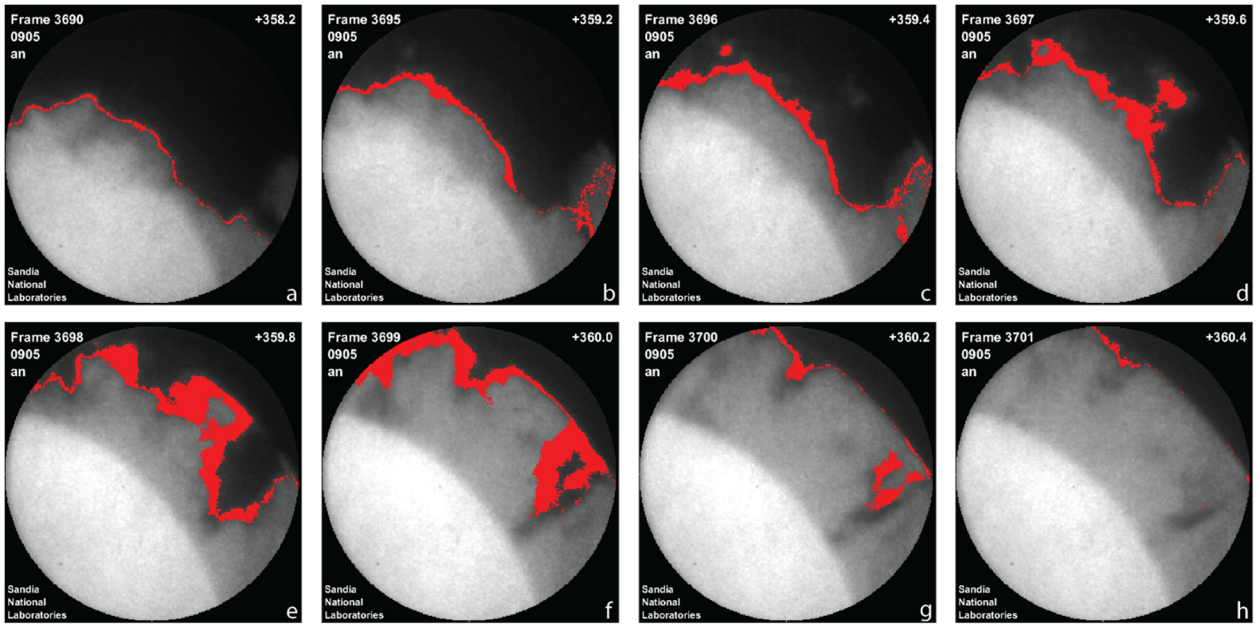

Figure 8. Sequence of OH* chemiluminescence images for a cycle where onset of knock occurs in the squish region and in close proximity to the propagating deflagration that precedes knock. See Figure 6 caption for display details.

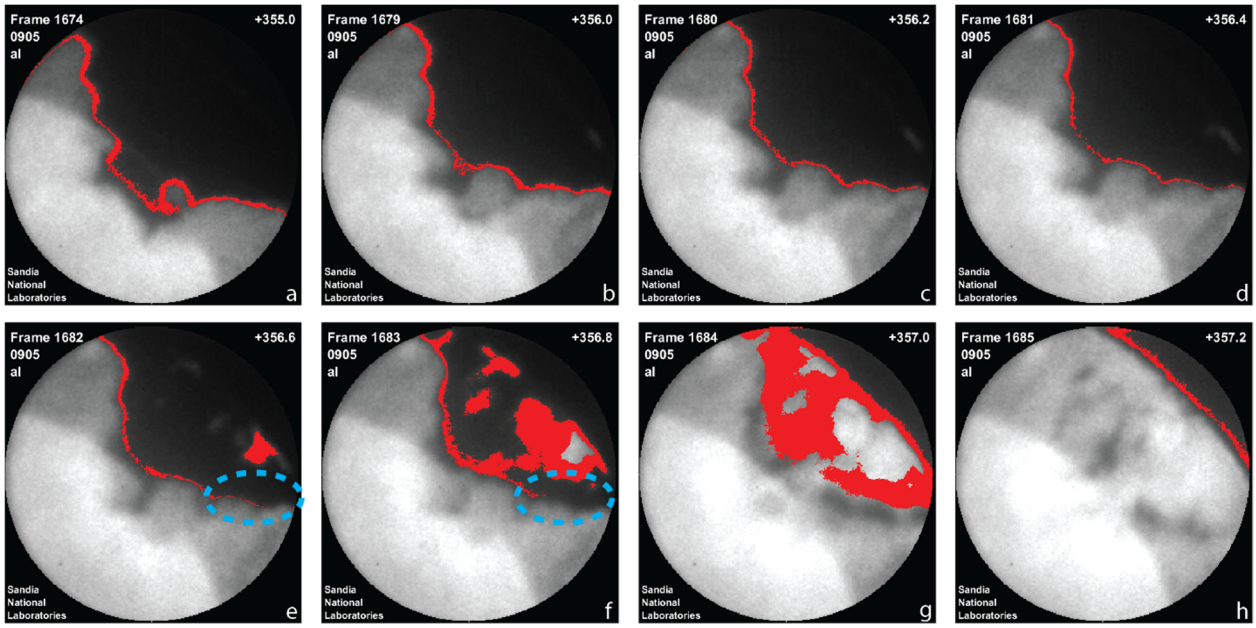

Figure 9. Sequence of OH* chemiluminescence images for a cycle where onset of knock occurs in near the crevice and isolated from the propagating deflagration that precedes knock. See Figure 6 caption for display details.

onset of knock. Again, expansion of the regions experiencing knock are likely displacing the deflagration backwards, such that the red ribbon indicating the change in position of the deflagration disappears. Finally, in image (g), the knocking rapidly consumes all or nearly off of the remaining unburned end-gas in the squish region.

Figure 10 shows a sequence of images for knock onset near the crevice but in closer proximity to the deflagration zone. Much like observed for squish-region knock in close proximity to the deflagration, the thickness of the red deflagration region thickens somewhat in image (c), prior to the rapid onset of knock in image (d). The broad red knock onset region quickly merges with the deflagration zone in the next image (e) and consumes the remaining unburned end-gas in the next three frames. As knock proceeds from image (c) to image (f), some thinning of the deflagration ribbon near the top of the images is apparent, again likely due to expansion in the knocking region displacing the deflagration region. However, such thinning is not apparent near the center of the image, where the red deflagration ribbon remains relatively thick.

Figure 11 shows a sequence of images where knock onset occurs in the bowl and somewhat isolated from the deflagration zone. Before discussing the character of knock for this image sequence, a different feature of pre-ignition is addressed first. In addition to capturing knocking combustion, the images in Figure 11 provide an example of local pre-ignition that creates a separate deflagration zone prior to the onset of knock. In the first image (a), a small new pocket of OH* chemiluminescence appears in the squish region separate from the existing deflagration zone. In the next image presented (b), which is one full degree crank-angle (ºCA) or five image frames later, this new deflagration zone has grown only slightly, and is surrounded by a thin red ribbon characteristic of the main deflagration zone and uncharacteristic of knock

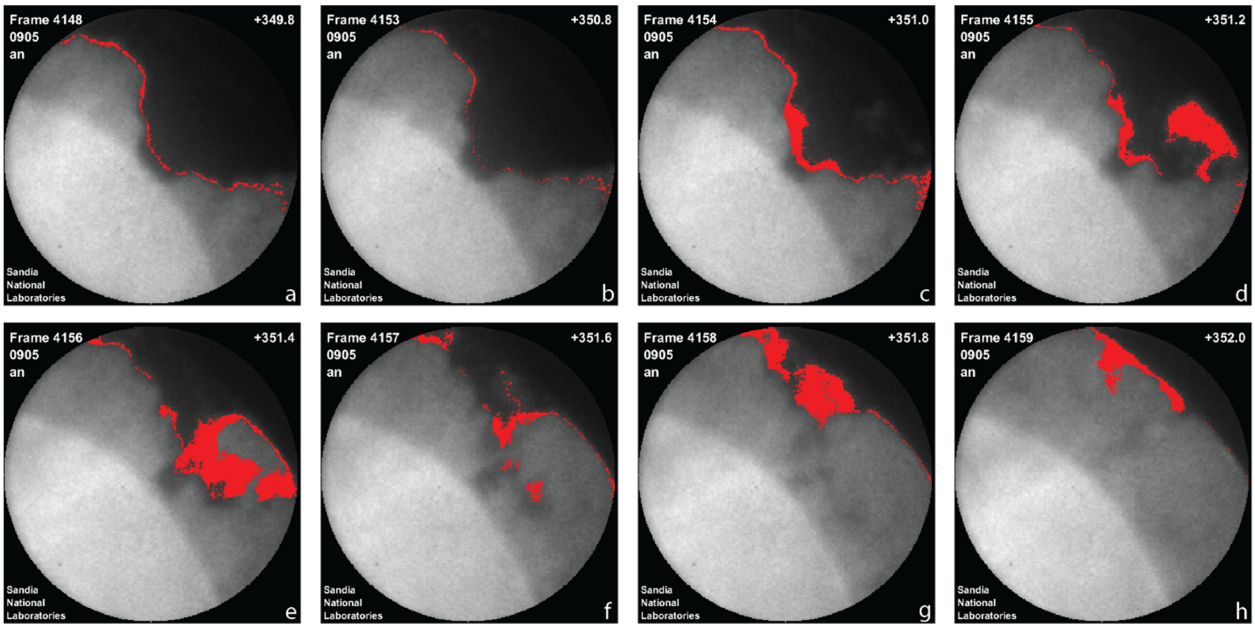

Figure 10. Sequence of OH* chemiluminescence images for a cycle where onset of knock occurs in near the crevice and in close proximity to the propagating deflagration that precedes knock. See Figure 6 caption for display details.

onset. The source of the pre-ignition is unclear, but it does not seem to immediately lead to the onset of knock. Instead, this pre-ignition deflagration propagates through the end-gas much like the main deflagration.

The onset of knock occurs in the fourth image (d), within the bowl and not obviously growing from the flame, though it does overlap with the flame. Because the knocking event occurs in the bowl, which is vertically much deeper (~21 mm) than the squish region (~5.5 mm), a much larger volume of unburned end-gas may be involved in the knocking event. Indeed, the rise in pressure and associated spike in the AHRR for both of the cycles in Figure 7 where the knock onset occurs in the piston bowl (bottom row) are larger than for any of the other conditions. And, the first cycle in Figure 7 (top-left) for the onset of knock in the squish region and isolated from the deflagration also has a significant portion of the transition to knock occurring in the bowl (see Figure 6) and a relatively large pressure rise and AHRR spike. Furthermore, the duration of the portion of the knock event in the bowl is much faster than observed for knock onset in the squish region or near the crevice, spanning only two frames (105 ms) compared to 4-6 frames (210-315 ms).

Also, much as in the other knocking cycles described above, the knocking zone displaces the deflagration zone, affecting the thickness of the red deflagration ribbon. In fact, because of the geometry of the deflagration zone, this displacement increases the thickness of the red deflagration ribbon on the side of the deflagration zone opposite the knocking region, while thinning it on the side facing the knocking region. This is consistent with a rightward displacement away from the knocking zone, as indicated by the blue arrows in Figure 11. And, likely because of the intensity of knocking in the large-volume piston bowl is larger than for the other cycles discussed

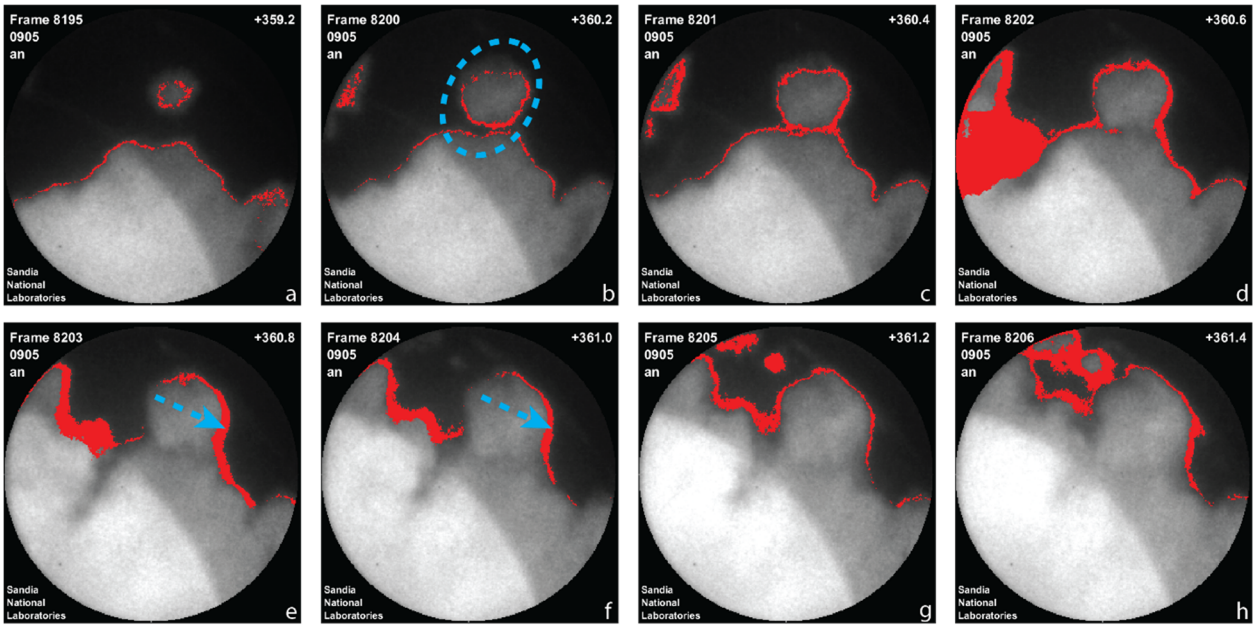

Figure 11. Sequence of OH* chemiluminescence images for a cycle where onset of knock occurs in the piston bowl and somewhat isolated from the propagating deflagration that precedes knock. See Figure 6 caption for display details.

thus far, the width of the ribbon on the far side appears larger due to greater displacement. The thickness of the ribbon on the left side of image (e) may also be due to displacement of the knocking region outward and into the squish region, which displaces as the existing deflagration in the squish region in the direction of the arrow. Also, in this particular cycle, combustion proceeds in the squish region more slowly relative to the other cycles presented here, with considerable unburned end-gas still remaining four image frames later.

Finally, Figure 12 shows a sequence of images with knock onset in the piston bowl in relatively close proximity to the deflagration zone. The third image (c) in the sequence shows a thickening of the red deflagration ribbon, followed by a rapid expansion of the red zone in the next image (d) as knocking develops. Much like the other piston-bowl knock-onset images in Figure 11, the images subsequent to the initial onset of knock show a slower consumption of the remaining unburned end-gas relative to the cycles with knock originating in the squish or crevice regions of Figure 6 through Figure 10. Also, as the knock progresses into the squish zone, a possible second knock onset occurs in the seventh image (g), which has a relatively large red zone, identified by the region within the dashed blue ellipse.

For the dataset included in this report, the onset of knock occurs most frequently in the squish region, in 61% of the knocking cycles observed. Second most common is knock originating in the bowl, at 51% of the time (individual cycles may display separate knock onset locations in multiple regions, so multiple characterizations may apply to a single image, such that the probabilities do not sum to 100%). Knock onset near the crevice between the piston and cylinder wall (upper-right of images; see Figure 5), is least common, occurring only 35% of the time.

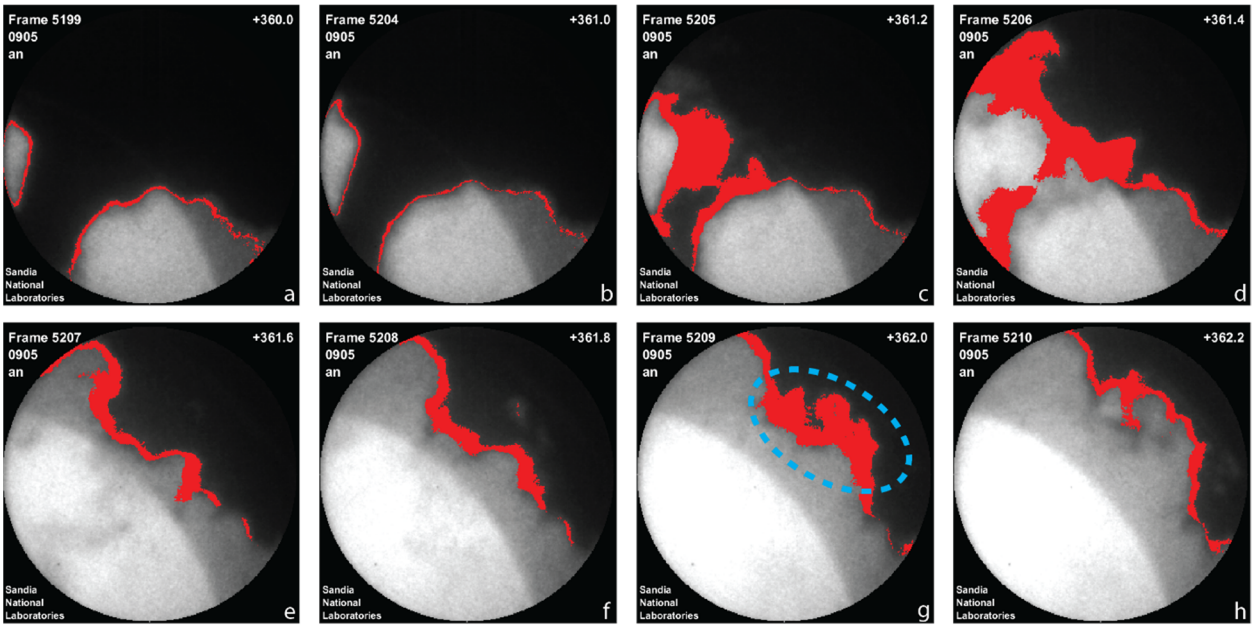

Figure 12. Sequence of OH* chemiluminescence images for a cycle where onset of knock occurs in the piston bowl and in close proximity to the propagating deflagration that precedes knock. See Figure 6 caption for display details.

3.2. Modeling Results

When this project was proposed, one expectation was that the ability of the 0-d model to accurately predict the timing of the onset of knock would depend on the spatial location of the onset of knock relative to in-cylinder surfaces and the deflagration zone. Under conditions with unburned end-gas remaining in the piston bowl, mixtures undergoing the onset of knock in the piston bowl and away from flame zones, such as the example in Figure 11, would be most consistent with the adiabatic assumption of the model. With a relatively small surface to volume ratio, and without significant interaction with the deflagration zone, the local mixtures at the onset to knock would be expected to be nearest to the adiabatic compression temperature assumed in the model. Of course, some small amount of heat transfer would likely reduce the temperature even in the hottest zones of the experiment, so the model using a higher temperature according to the fully adiabatic assumption might predict a slightly earlier onset of knock. This expectation of the comparison between model predictions and experimental measurements of the knock onset is illustrated notionally in Figure 13. The narrow bright red band located slightly below the 1:1 agreement line for the model predictions represents the expectation of a slightly early predicted knock onset by the model when it occurs in the piston bowl and isolated from the deflagration zone (flame) in the experiments.

Alternatively, if the onset of knock were to occur near the deflagration zone, such as for the example cycle in Figure 12, and if such proximity were to affect the onset of knock, the model-predicted knock timing would be expected not to match the experimentally measured knock onset as well, since the model would not account for additional factors that affect the onset of knock in such situations, such as heat and

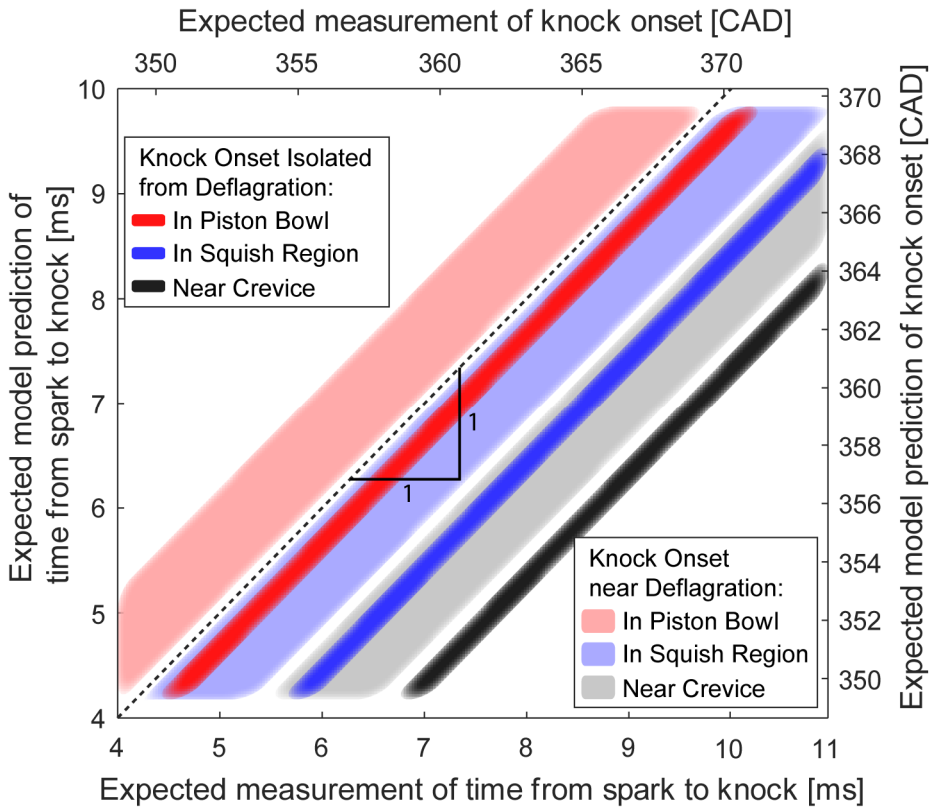

Figure 13. Expectations for comparison of model-predicted knock onset timing to experimental measurements for six different characterizations of knock onset according to the location within the combustion chamber and proximity to the deflagration zone.

mass transfer from the flame zone. Additionally, the degree of interaction with the flame might vary from cycle to cycle depending on various in-cylinder factors, such that the variability in the timing of the knock onset would vary more from one cycle to the next. These expectations are illustrated graphically in Figure 13 as the light-red band that is shifted to the left of the bright red band, to represent an shift to earlier timings for the experimental measurements, and with a greater width than the bright red band, representing a greater variability from cycle to cycle.

For cycles where unburned gas in the piston bowl has been consumed before knock could occur, the onset of knock might occur in the squish region where some end-gas remains, such as the example cycle in Figure 6. With much closer proximity to the cylinder head and piston top for the squish region, the model-predicted knock onset would also fail to match the experimental observations due to heat-transfer losses to the wall not consistent with the adiabatic assumption of the model. This expectation is represented graphically in Figure 13 as a narrow bright blue band, shifted to the right to reflect later measured knock onset. Once more, if knock onset is near a flame zone in the crevice region, additional factors would affect the timing and variability of the onset of knock, and model predictions would also be less accurate, as represented by the wide light-blue band in Figure 13. Similar expectations existed for knock onset

near the crevices, such as the example cycles in Figure 9 (isolated from the deflagration zone) and Figure 10 (in closer proximity from the flame zone), with heat transfer losses to the wall likely being even greater due to the narrow width of the crevice region. These expectations for knock onset in or near the crevice region are represented by the black (isolated from the deflagration) and gray (near the deflagration) bands in Figure 13.

To compare the model-predicted knock-onset timing to that of the experiments, the indicator of the onset of knock must be defined for each. For the experimental data, the onset of knock is defined according to the AHRR data, such as the red curves in Figure 7. As described earlier, the onset of knock is associated with the narrow spike in the AHRR curve after the broader rise and fall in the AHRR associated with the deflagration combustion. Hence, the onset of knock in the experiments is taken as the leading edge of the narrow spike, which is defined here as the time prior of the peak of the spike where the rate of change in the AHRR exceeds 20 J/CAD^2. This threshold was selected somewhat subjectively, and was found to yield reasonable agreement between that selected by an algorithm and visual inspection to locate the sharp leading edge of the knocking AHRR spike. The open circles on the experimental pressure and AHRR curves in Figure 7 are those calculated by this algorithm, and they indicate the leading edge of the AHRR spike well in all cycles examined here.

For the model, the knocking threshold is taken as the time when the predicted temperature exceeds 1200 K, which has been recommended as an indicator of the transition to high-temperature chemistry [35].

With the onset of knock precisely defined for the models and the experiments, the values of each may be compared. Contrary to the expectations discussed above and illustrated in Figure 13, the model predictions for the three state-of-the-art chemical kinetics mechanisms [30, 31, 33] described in Section 2.6, as well as the older but more historically significant GRIMech30 mechanism [34], matched the experimental predictions surprisingly well. As shown in Figure 14, the predictions of the modern 2018 Miller [30], 2017 Aramco/Galway [31], and 2016 CSU [33] mechanisms aligned very well with the 1:1 line versus the experimental measurements. The predictions of the much older GRI mechanism [34] lagged the experimental measurements more than the other models, but the trend is quite similar.

One potential artifact that may explain the excellent agreement and that merits discussion is feedback from the measured cylinder pressure trajectory that constrains the 0-d model. It is conceivable that the rise in pressure that occurs at the onset of knock compresses the gas in the model, raising its temperature and forcing a transition to knock that would not have otherwise occurred, such that the model predictions will always agree with experiments. While this may indeed occur for some conditions, for the data in this study, this is not the case. Figure 15 shows an expanded plot of the cylinder pressure from the knocking cycles of the six cycles characterized above according to the spatial location of the onset of knock, as well as the “outlier” data point in Figure 14 that is farthest from the 1:1 line (latest predicted knock onset relative to the measured knock onset). For each cylinder pressure curve, the onset of knock as predicted by the Miller chemical kinetic mechanism [30] is plotted on the

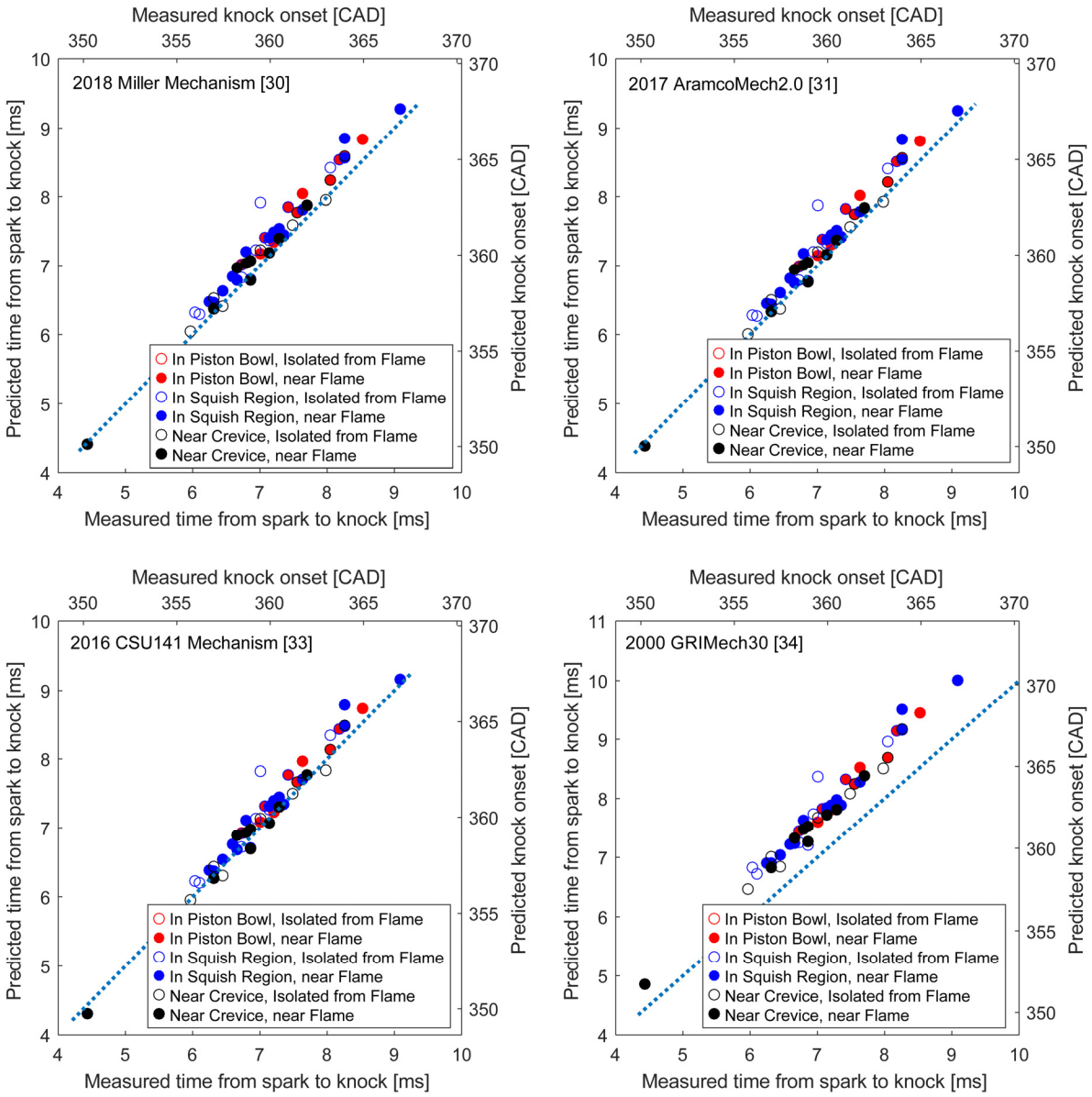

Figure 14. Comparison of model-predicted knock onset to experimental measurements for four chemical kinetic mechanisms as indicated on each plot.

pressure curve as an open circle. Figure 15 shows that for all six cycles highlighted above, as well as for the outlier cycle, the measured pressure trajectory that is an input to the 0-d model does not change its trajectory due to the pressure rise associated with knocking combustion until after the model has already crossed the 1200 K threshold that defines the onset of knock. Indeed, the blue curves in Figure 11, which show the model-predicted heat release rate (due to knock only*) for each of the six characteristic

* The simulations predict heat release only from the knocking event and not from the deflagration, and hence the blue curves in Figure 11 can only be directly compared to the narrow spikes in the red curves of the measured AHRR that are associated with knock.

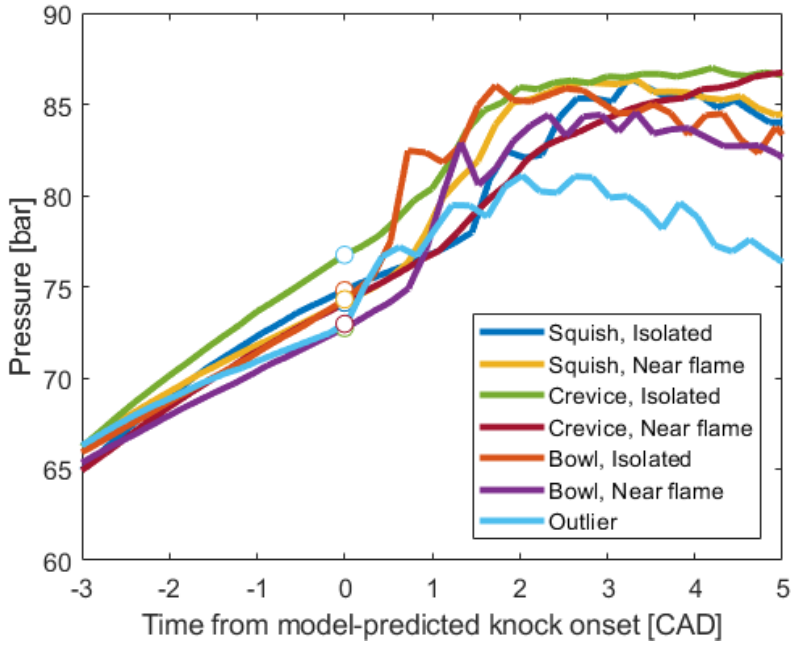

Figure 15. Cylinder pressure near the onset of knock for a selected cycle with knock occurring in the piston bowl and isolated from the flame (corresponding to images in Figure 11). The symbol is placed at the time of the onset of knock predicted by the 2018 Miller chemical kinetic mechanism [30].

types of knocking onset begins rising several ºCA before the pressure rise associated with knock, and hence is already "committed" to knocking as the reaction rate is accelerated. Hence, for the experimental data and model predictions presented here using any of the three recent chemical kinetic mechanisms shown in Figure 14, cylinder pressure feedback from the knocking event in the experiments does not affect the predicted onset of knock in the models. Because of its later prediction of knock, the GRI mechanism [34] is affected to some degree by this knocking-pressure feedback.

One likely contributor to the excellent agreement is the precise definition of the natural gas composition used in the experiments, which is a critical input to the model. As described in Section 2.4, the experiments were designed to use a certification-grade synthetic natural gas mixture, for which the uncertainties in the concentrations of the ethane and propane components is ±2% (relative). Most prior experimental data from natural gas engines used fuels with higher composition uncertainties, which would affect model fidelity.

The comparison in Figure 14 supports an important conclusion that at least for the fuel composition and operating conditions explored in this project, existing state-of-the-art chemical kinetics mechanisms have sufficient fidelity to predict the onset of knock if the deflagration and subsequent in-cylinder pressure trajectory is properly modeled.

Furthermore, the good agreement between the predictions and the measurements was insensitive to the character of the onset of knock in terms of the proximity to walls or

the deflagration zone. Nearly all of the predictions for the three recent chemical kinetics mechanisms fell within a ±0.1 ms band along the 1:1 line. Though delayed by approximately 0.5 ms from the 1:1 line, the older GRI mechanism maintained a similarly tight grouping regardless of the characteristics of the onset of knock. This observation of a lack of sensitivity to the character of the onset of knock leads to a second important conclusion that an adiabatic assumption works well for predicting knock even when heat transfer from nearby walls or heat/mass transfer from deflagration regions might be expected to affect the onset of knock.

From these two conclusions, it follows that for the fuel composition and conditions explored in this project, further effort to improve chemical-kinetic mechanism fidelity is unnecessary – the existing validation methods based on measurements from flames, shock tubes, rapid compression machines, and other experiments are already sufficient for application to in-cylinder combustion in an engine. Instead, the inability of engine design models to reliably predict knock must lie elsewhere, most likely in their fidelity in predicting the cylinder pressure trajectory and/or local mixing state. Hence, further research should be directed toward developing a science base on the factors that affect the cylinder-pressure trajectory and fuel-air mixture distribution, including spark ignition dynamics and flame kernel growth, flame development, in-cylinder flow and geometry effects, and mixture preparation effects.

4. SUMMARY

This project successfully designed and built new experimental facilities for optical engine research on natural gas combustion and utilized them in parallel with a chemical-kinetic model of autoignition to answer a key science question, closing a gap in the science base for natural gas combustion. The new research facility provides the capability to safely pressurize natural gas to as high as 650 bar-g, which is high enough to satisfy the requirements of all current natural gas engine approaches, as well as anticipated future directions in natural gas engines. The facility also provides a means to recover and safely store natural gas from the engine fuel-delivery infrastructure so that expensive, long lead-time certification-grade natural gas may be efficiently used, enabling repeatable operating conditions and measurements with lower uncertainty.

Experimental facility enhancements also include a new engine research capability for safely fueling a heavy-duty optical engine with natural gas across all current approaches (fumigated premixed, direct-injected premixed, high-pressure direct injection, dual-fuel), as well as more advanced concepts such as low-temperature compression ignition and turbulent jet ignition.

Using these new facilities, experimental data including cylinder pressure and high-speed OH* chemiluminescence imaging were acquired under laser-spark-ignited knocking conditions fueled with a synthetic natural gas mixture with well-defined minor species concentrations. Visual inspection of the OH* chemiluminescence images allowed characterization of the knock onset for individual cycles according to the proximity to in-cylinder surfaces and the laser-spark-ignited deflagration zone. Additionally, a zero-dimensional chemical-kinetic model constrained by the measured

cylinder-pressure trajectory and using an adiabatic simplification was employed to predict the timing of the onset of knock relative to the experiments. Contrary to expectations, model predictions of the timing of the knock onset agreed well with the measurements regardless of the character of knock.

These observations support the conclusion that for the fuel composition and in-cylinder conditions explored in this project, further effort to improve chemical kinetic mechanism fidelity is unnecessary. Instead, further research should be directed toward developing a science base on the factors that affect the cylinder pressure trajectory and fuel-air mixture distribution, including spark-ignition dynamics and flame-kernel growth, flame development, in-cylinder flow and geometry effects, and mixture preparation effects.

REFERENCES

1. US Energy Information Administration, *Monthly Energy Review*, DOE/EIA-0035(2018/8), https://www.eia.gov/totalenergy/data/monthly/pdf/mer.pdf, August 2018.
2. BP, *Statistical Review of World Energy, 67th Ed.*, bp.com/en/global/corporate/energy-economics/statistical-review-of-world-energy.html, June 2018.
3. Hekkerta MP, Hendriska FHJF, Faaijb, APC, Neelisb ML, *Natural Gas as an Alternative to Crude Oil in Automotive Fuel Chains Well-to-Wheel Analysis and Transition Strategy Development*, Energy Policy 33(5):579–594, 2005.
4. Tiax LLC / California Energy Commission, *Full Fuel Cycle Assessment: Well-to-Wheels Energy Inputs, Emissions, and Water Impacts*, Report #CEC-600-2007-004-F, 2007.
5. Askin AC, Barter GE, West TH, Manley DK, *The Heavy-Duty Vehicle Future in the United States: A Parametric Analysis of Technology and Policy Tradeoffs*, Energy Policy 81:1–13, 2005.
6. New West Technologies LLC / US DOE, *Clean Cities Alternative Fuel Price Reports*, http://www.afdc.energy.gov/publications/search/keyword/?q=alternative fuel price report, 2011-2016.
7. Zigler B, *Possible Pathways for Increasing Natural Gas Use for Transportation*, Natural Gas Vehicle Technology Forum, Wilmington CA, 15 October 2015.
8. Figer G, Seitz HF, Graf G, Schreier H, *Commercial Vehicle Natural Gas Engines with Diesel Efficiency*, MTZ Worldwide 75(10):1-15, 2014.
9. Cornwell R, Foster D, Noble A, *Natural Gas and Dual Fuel Engine Technologies for HDV*, IMechE Seminar S1807, London UK, 2014.
10. Hampson G, *Personal Communication*, Woodward Engine Control Systems, 2015.
11. Dec JE, *A Conceptual Model of D.I. Diesel Combustion Based on Laser-Sheet Imaging*, SAE Tech. Paper 970873, SAE Trans. 106(3):1319-1348, 1997.
12. Musculus MPB, Miles PC, Pickett LM, *Conceptual Models for Partially Premixed Low-Temperature Diesel Combustion*, Prog. Energy Combust. Sci. 39(2):246-283, 2013.
13. Link AN, *Retrospective Benefit-Cost Evaluation of US DOE Vehicle Combustion Engine R&D Investments: Impacts of a Cluster of Technologies*, prepared by U. of North Carolina for US DOE, https://www1.eere.energy.gov/analysis/pdfs/advanced_combustion_report.pdf, 2010.
14. Stanton DW, *Systematic Development of Highly Efficient and Clean Engines to Meet Future Commercial Vehicle Greenhouse Gas Regulations*, SAE Technical Paper 2013-01-2421, SAE Int. J. Engines 6(3):1395-1480, 2013.
15. Zur Loye, A, Personal Communication, Cummins Inc, 2016.
16. Zádor J, Taatjes CA, Fernandes RX (2011), Kinetics of Elementary Reactions in Low-Temperature Autoignition Chemistry, Prog. Energy Combust. Sci. 37(4):371-421.
17. Stewart K, *Natural Gas (NG) Source Manifold-906/165 Pressure Safety Data Package & Operational Guidelines*, Sandia National Laboratories, 2017.

18. *Maximator Technical Data Sheet - Gas Booster DLE 15-75-2*, Maximator GmbH, 2005.

19. Musculus MPB, *Standard Operating Procedure (SOP), Sandia/Cummins Diesel Engine Laboratory,* Sandia National Laboratories SOP SP1986-G, 2016.

20. *Maximator Technical Data Sheet - Gas Booster DLE 2-5*, Maximator GmbH, 2005.

21. Stewart K, *Pressure Data Package for Portable Vacuum Station,* Sandia National Laboratories, 2016.

22. Stewart K, *Natural Gas (NG) Delivery Manifold Pressure Safety Data Package & Operational Guidelines,* Sandia National Laboratories, 2018.

23. Garcia A, *Fuel Tracer Vaporizer System Pressure Data Package*, Sandia National Laboratories, 2017.

24. Floyd LD, Morrison LS, et al., *NFPA 68: Standard on Explosion Protection by Deflagration Venting*, National Fire Protection Association, 2018.

25. Pastor TP, Roberts SC, et al., *2017 ASME Boiler and Pressure Vessel Code, SECTION VIII – Rules for Construction of Pressure Vessels*, ASME BPCV.VIII.1-2017, American Society of Mechanical Engineers, Two Park Avenue, New York, NY 10016-5990, 2017.

26. Pastor TP, Roberts SC, et al., *2017 ASME Boiler & Pressure Vessel Code, SECTION II – Materials Part D, Properties (Metric)*, ASME BPCV.II.D.M-2017, American Society of Mechanical Engineers, Two Park Avenue, New York, NY 10016-5990, 2017.

27. Musculus MPB, Dec JE, Tree DR, *Effects of Fuel Parameters and Diffusion Flame Lift-Off on Soot Formation in a Heavy-Duty Diesel Engine*, SAE Paper 2002-01-0889, SAE Transactions, 111, No. 3, pp. 1467-1489, 2002.

28. Gaydon AG, *The Spectroscopy of Flames*, London, England, Chapman and Hall Ltd., 1974.

29. *CHEMKIN-PRO 18.1*, Reaction Design, San Diego, 2013.

30. Miller JA, *C0-C3 Chemical Kinetic Mechanism with Prompt HCO Chemistry*, unpublished, 2018.

31. Li Y, Zhou C-W, Somers KP, Zhang K, Curran HJ, *The Oxidation of 2-Butene: A High Pressure Ignition Delay, Kinetic Modeling Study and Reactivity Comparison with Isobutene and 1-Butene*, Proc. Combust. Inst. 36(1):403–411, 2017.

32. Zhang K, Banyona C, Bugler J, Curran HJ, Rodriguez A, Herbinet O, Battin-Leclerc F, B'Chir C, Heufer KA, An updated experimental and kinetic modeling study of n-heptane oxidation, Combust. Flame 172:116-135, 2016.

33. Hockett A, Hampson G, Marchese AJ, Development and Validation of a Reduced Chemical Kinetic Mechanism for Computational Fluid Dynamics Simulations of Natural Gas/Diesel Dual-Fuel Engines, Energ. Fuels 30(3):2414-2427, 2016.

34. Smith GP, Golden DM, Frenklach M, Moriarty NW, Eiteneer B, Goldenberg M, Bowman CT, Hanson RK, Song S, Garidner WC Jr., Lissianski VV, Shiwei Q, *GRIMech30*, http://www.me.berkeley.edu/gri_mech/, 2000

35. Westbrook CK, *Chemical Kinetics of Hydrocarbon Ignition in Practical Combustion Systems*, Proc. Combust. Inst. 28:1563-1577, 2000.

36. Graham T, *On the Motion of Gases,* Phil. Trans., v. 136:573-631, 1846.

37. Engineering Equation Solver (EES), F-Chart Software, Madison, WI, 2018

38. Bartknecht W, *Explosions: Course Prevention Protection*, Springer-Verlag, New York, 1981.

APPENDIX A: EXHAUST PLENUM DEFLAGRATION VENTING CALCULATIONS

Though unlikely to occur, under certain failure scenarios, it is possible that the exhaust plenum could be filled, fully or partially, with a mixture capable of supporting a flame. Even with precautions to eliminate ignition sources (i.e., flame arrestor at engine exhaust port), the possibility of ignition from some unanticipated source and the resulting pressure upon combustion of the flammable mixture in the exhaust plenum must be considered.

To relieve the rise in pressure that a flammable gas ignition and subsequent combustion event might generate, the exhaust plenum is equipped with a burst disk, properly sized to provide sufficient flow to prevent overpressure of the plenum that would cause it to be damaged or to rupture. This appendix describes the standardized calculations for sizing of that burst disk, according to the NFPA68 Standard on Explosion Protection by Deflagration Venting [24]. Afterwards, the ability of the exhaust plenum to withstand pressures generated during vented deflagration is assessed.

Important specifications of the exhaust plenum are provided in Table A3.

To determine the relevant section of NFPA68 [24] for the venting burst disk size calculations, the pressure reached during a deflagration event and the inertia of the "vent closure" (in this case, a burst disk) must be considered. Regarding the developed pressure, on page 68-8 of NFPA68 [24], the reduced pressure P_{red} is defined as "the maximum pressure developed in a vented enclosure during a vented deflagration." P_{red} is considered high when it exceeds 0.5 bar-g. P_{red} must be determined through an iterative calculation as described below, and the result of the calculation is that P_{red} has a value of 4.13 bar-g, and hence is considered high. Regarding the vent closure inertia, page 68-41 of Annex A of NFPA68 [24] considers a rupture diaphragm as an "inertialess vent closure." Hence, the relevant section for calculations of the pressure developed during vented

Table A3. Exhaust Plenum Specifications

Material	SA240 - GR304 stainless steel
Internal diameter, D_i [m]	0.4064
Internal height, L_i [m]	1.2033
Wall thickness, t_w [m]	0.00635
Elliptical cap aspect ratio [-]	2:1
Elliptical cap nominal wall thickness, t_c [m]	0.00794
Circumferential joint efficiency, E_c [-]	0.45
Longitudinal joint efficiency, E_l [-]	0.70
Exhaust runner diameter, D_r [m]	0.0762
Burst disk vent diameter D_v [m]	0.0762
Nominal vent burst pressure [psi-g]	4±1.5

deflagration in the exhaust plenum is section 7.2.2 on page 68-15, "Low Inertia Vent Closure Equations for High P_{red}."

According to equation 7.2.2a [24] of that section, the required vent area can be expressed as

$$A_{v0} = A_s \frac{\left[1-\left(\frac{P_{red}+1}{P_{max}+1}\right)^{1/\gamma_b}\right]}{\left[\left(\frac{P_{red}+1}{P_{max}+1}\right)^{1/\gamma_b}-\delta\right]} \frac{S_u \rho_u}{G_u} \frac{\lambda}{C_d}, \quad \text{(A1)}$$

where

$$\delta = \frac{\left(\frac{P_{stat}+1}{P_0+1}\right)^{1/\gamma_b}-1}{\left(\frac{P_{max}+1}{P_0+1}\right)^{1/\gamma_b}-1} \quad \text{(A2)}$$

and

A_{v0} = the vent area calculated from Equation A1 [m^2]
A_s = the exhaust plenum internal surface area determined according to Equation A3 [m^2]
P_{red} = the maximum pressure developed in the vented exhaust plenum during a vented deflagration [bar-g]
S_u = fundamental burning velocity of the natural-gas-air mixture [m/s]
ρ_u = mass density of the unburned natural-gas-air mixture
λ = ratio of the natural-gas-air mixture burning velocity accounting for turbulence and flame instabilities in vented deflagration to the fundamental (laminar) burning velocity determined according to Equation A4
G_u = unburned natural-gas-air mixture sonic-flow mass-flux [kg/m^2-s]
C_d = vent flow discharge coefficient [-]
P_{max} = the maximum pressure developed in a contained deflagration by ignition of the same natural-gas-air mixture [bar-g]
P_0 = the enclosure pressure prior to ignition [bar-g]
γ_b = ratio of specific heats for burned natural-gas-air mixture
P_{stat} = nominal vent burst pressure [bar-g]

As described in section 7.2.5.1 on page 68-16 of NFPA68 [24], the enclosure surface area A_s "shall include the total area that constitutes the perimeter surfaces of the enclosure that is being protected," which for a cylindrical tank can be expressed as

$$A_s = 2\pi {D_i}^2/4 + \pi D_i L_i = 1.796\ [m^2], \quad \text{(A3)}$$

where

D_i = exhaust plenum internal diameter, from Table A3 [m]
L_i = exhaust plenum internal height, from Table A3 [m].

The nominal vent burst pressure as certified by the manufacturer is 4±1.5 psi-g. Taking the worst-case rupture pressure of 4+1.5 = 5.5 psi-g yields P_{stat} = 0.38 bar-g. There is no significant

restriction between the exhaust plenum and the roof vent, and prior measurements show that the pressure in the exhaust plenum never exceeds 1 psi-g. As a conservative estimate, P_0 is taken as 0.1 bar-g (1.45 psi-g). The fundamental burning velocity of the natural-gas-air mixture S_u is taken as that of methane, the majority component (~95%) in natural gas, in Table D.1 on page 68-70 [24], as 0.4 m/s. The mass density of the unburned natural-gas-air mixture ρ_u is given according to the recommendation in section 7.2.3.3 using 1.2 kg/m^3 for mixtures up to 5 vol % stoichiometric concentration. (This is a conservative estimate because natural gas has a lower molecular weight than air, and hence the density at stoichiometric conditions near 10 vol % natural gas will be lower than 1.2 kg/m^3.)

The burning velocity ratio λ is given on page 68-17 of NFPA68 [24]:

$$\lambda = \lambda_1 \left[1 + \left(\frac{L_i/D_i}{2.5} - 1 \right)^2 \right], \tag{A4}$$

where λ_1 is the enhanced burning velocity ratio in the presence of internal structures. Equation A4 strictly applies only for values of P_{red} of 2 bar-g or less, but no other estimate is available, so Equation A4 is used with appropriate caveat. Given that the exhaust plenum has no internal structures, λ_1 can be taken as the baseline burning velocity ratio λ_0, given on page 68-17 of NFPA68 [24] as:

$$\lambda_0 = \varphi_1 \varphi_2 \tag{A5}$$

where

$$\varphi_1 = \left(\frac{Re_f}{4000} \right)^{0.39} \tag{A6}$$

$$\varphi_2 = max \left\{ 1, 1.23 \left(\frac{Re_v}{10^6} \right)^{\left(\frac{0.00237}{S_u} \right)^{0.5}} \right\} \tag{A7}$$

$$Re_f = \frac{\rho_u S_u (D_{he}/2)}{\mu_u} \tag{A8}$$

$$Re_v = \frac{\rho_u u_v (D_v/2)}{\mu_u} \tag{A9}$$

$$u_v = min \left\{ \sqrt{\frac{2 \cdot 10^5 P_{red}}{\rho_u}}, a_u \right\} \tag{A10}$$

and

D_{he} = the exhaust plenum hydraulic equivalent diameter [m]
μ_u = the unburned natural-gas-air mixture dynamic viscosity [kg/m-s]
D_v = the vent diameter [m]
u_v = the maximum velocity through the vent
a_u = the unburned natural-gas-air mixture sound speed [m/s]

According to section 6.4.3 on page 68-12 of NFPA68 [24], the hydraulic equivalent diameter D_{he} of a cylindrical vessel can be taken as the vessel diameter D_i, which is given in Table A3 for the exhaust plenum. The unburned natural-gas-air mixture dynamic viscosity μ_u was estimated according to the mole fractions [36] of natural gas and air at stoichiometric conditions as 1.8×10^5 kg/m-s, which is identical to two significant digits as the recommendation in section 7.2.3.6 on page 68-16 of NFPA68 [24]. Using these values, the Reynolds number of the flame propagation across the diameter of the exhaust plenum Re_f in Equation A8 is 5400, which yields $\varphi_1 = 1.13$. Using ideal gas relationships, the unburned natural-gas-air mixture sound speed a_u may be calculated as

$$a_u = \sqrt{\gamma \bar{R} T / M} \tag{A11}$$

where

$\gamma =$ the mixture specific heat ratio
$\bar{R} =$ the universal gas constant [kJ/kmol-K]
$T =$ the gas temperature [K]
$M =$ the mixture molecular weight [kg/kmol]

For a stoichiometric mixture of methane and air, M=27.7 kg/kmol, and at T=150 ºC (423 K), the EES thermodynamics code [37] can be used to calculate γ as 1.357. Then, using $\bar{R}$=8.314 kJ/kmol-K, the speed of sound is a_u=363 m/s. Using a value of P_{red}=4.13 bar-g, the maximum velocity through the vent u_v is equal to a_u. The vent Reynolds number is then $Re_v = 9.22 \times 10^5$, φ_2=1.22, $\lambda_1 = \lambda_0$=1.38, and λ=1.42.

For stoichiometric natural-gas-air combustion products at 2000 K, the burned-gas specific heat ratio is γ_b=1.25. The maximum pressure of a contained deflagration for a natural-gas-air mixture initially at 0 bar-g is taken from that of methane in Table D.2 on page 68-71 of NFPA68 [24] as 7.1 bar-g, and is adjusted according to the absolute pressure ratio using the starting pressure P_0 in the exhaust plenum:

$$P_{max} = \left(P_{max,0\ bar-g} + 1\right) \cdot (P_0 + 1) - 1 = 7.9 \text{ bar-g} \tag{A12}$$

Equation A2 can then be evaluated to yield δ=0.0458. Using a value of 0.7 for the discharge coefficient C_d, as recommended in section 7.2.4.1 on page 68-16 of NFPA68 [24], Equation A1 can be evaluated as A_{v0}=0.00456 m^2, which corresponds to a vent diameter of D_v=0.0762 m, matching the value listed in Table A3. As described earlier, this match was achieved through an iterative calculation, varying the value of P_{red} until the required vent diameter matched the physical vent diameter, at P_{red} = 4.13 bar-g.

The above solution to Equation A1 applies to relatively low turbulence levels, for which the maximum velocity in the vessel is 5 m/s or less. If the connected piping of the exhaust runner delivers gas at a velocity higher than 5 m/s, then the above solution to Equation A1 does not strictly apply.

For a reciprocating internal combustion engine, the average flow velocity U_r in the exhaust runner connected the to exhaust plenum under non-combusting conditions where the exhaust plenum could be filled with unburned flammable gas can be calculated by

$$U_r = \frac{V_d(S_i/60/2)(P_{int}+1)/(P_0+1)}{\pi {D_r}^2/4} \tag{A13}$$

where

V_d = the engine displacement [m^3]
S_i = the engine crankshaft speed [RPM]
P_{int} = the intake pressure [bar-g]
D_r = the exhaust runner internal diameter [m].

Using the engine displaced volume V_d from Table 1, the experimental running speed S_i = 1200 rotations per minute (RPM), the highest achievable intake pressure P_{int} = 2 bar-g, and D_r from Table A3, the average exhaust runner flow velocity is 14 m/s, which is above the threshold at which turbulence enhancement should be considered. Unfortunately, NFPA68 [24] does not provide recommendations on the degree of turbulence enhancement to lambda provided by this inlet flow velocity. Hence, using the above calculations as the best available estimate, for a burst disk diameter of 0.0762 m (3 inches), the vented pressure for a stoichiometric natural-gas-air mixture initially at 0.1 bar-g is 4.13 bar-g.

Note that the value of 4.13 bar value of P_{red} is for a 100% fill factor of stoichiometric natural gas and air in the exhaust plenum, which is an extremely unlikely scenario. A more likely scenario is a fraction of misfired cycles that partially fill the exhaust plenum with flammable gas. Under such conditions, the required vent area is smaller, and can be calculated as according to the following equation from section 8.4.1 on page 68-21 of NFPA68 [24]

$$A_{vX} = A_{vLD} {X_r}^{-1/3} \sqrt{\frac{X_r - P_{red}/P_{max}}{1 - P_{red}/P_{max}}} \tag{A14}$$

Where

A_{vX} = vent area required for partial volume deflagration [m^2]
A_{vLD} = vent area required for Li/Di>2 [m^2]
X_r = fill fraction

Section 8.4.1.1 of the NFPA68 [24] also advises that when $X_r < P_{red}/P_{max}$, deflagration venting is not required at all, which corresponds to misfiring half the cycles or fewer, which is typical of anticipated experiments. Hence, only under very unusual conditions of fueling and misfiring over 50% of engine cycles will a hazard be present, which would be outside the bounds of all anticipated experiments. Nevertheless, deflagration venting is implemented.

With the reduced pressure P_{red} determined, the ability of the exhaust plenum to withstand that pressure must be evaluated. The American National Standard document "2017 ASME Boiler and Pressure Vessel Code, SECTION VIII – Rules for Construction of Pressure Vessels" (ASME BPVC8) [25] provides standard calculation methods for such evaluation.

As described in section UG-27 on page 18 of the ASME-BPVC8 [25], the allowable stress on both circumferential and longitudinal welded joints, as well as the ellipsoidal heads of the pressure vessel, must be considered. For the longitudinal joints, the internal design pressure may be calculated as

$$P_d = \frac{S_m E_l t}{D_i/2+0.6t} \tag{A15}$$

Where

P_d = internal design pressure [bar]
S_m = maximum allowable stress value [bar]
E_l = longitudinal joint efficiency for, or the efficiency of, appropriate joint in cylindrical or spherical shells, or the efficiency of ligaments between openings, whichever is less
t = The thickness of the shell [m]

The cylindrical butt-joints of the exhaust plenum are weld-through but without radiographic exam, for which the recommended joint efficiency in Table UW-12 on page 117 of the ASME-BPVC8 [25] is 0.7. The shell thickness is provided in Table A3.

The maximum allowable stress S_m for many common pressure vessel materials may be found in a companion document, the American National Standard document "2017 ASME Boiler & Pressure Vessel Code II Materials Part D Properties (Metric)" (ASME-BPVC2) [26]. For the exhaust plenum material listed in Table A3, the maximum allowable stress at various temperatures may be found in Table 1A starting on page 86, row 30 of ASME-BPVC2 [26]. Three temperatures of interest are 150 ºC, 750 ºC, and 1500 ºF (815 ºC). The first is the highest temperature that would be reached under misfiring conditions where the exhaust plenum could be filled with flammable unburned fuel. The second is near the maximum temperature at which the design pressure still exceeds *P*red. The third temperature is that of the certified rating for the tank, which is useful for comparison to calculations.

At these three temperatures, row 30 of Table 1A on pages 88 and 89 of ASME-BPVC2 [26] gives the following values, which yield the corresponding design pressures for the longitudinal joints, according to Equation A15:

S_m (150 ºC) = 1030 [bar]; P_d (150 ºC) = 22.1 [bar-g]
S_m (725 ºC) = 213 [bar]; P_d (725 ºC) = 4.57 [bar-g]
S_m (815 ºC) = 96.2 [bar]; P_d (815 ºC) = 2.07 [bar-g]

For the circumferential joints, the internal design pressure may be calculated as

$$P_d = \frac{2S_m E_c t}{D_i/2-0.4t} \tag{A16}$$

Where

E_c = circumferential joint efficiency for, or the efficiency of, appropriate joint in cylindrical or spherical shells, or the efficiency of ligaments between openings, whichever is less.

For the circumferential joint, melt-through is not specified by the manufacturer, so that joint efficiency is taken as that supplied by the manufacturer and listed in Table A3. The resulting design pressures for the circumferential joints at the three temperatures of interest are:

P_d (150 ºC) = 29.3 [bar-g]
P_d (725 ºC) = 6.07 [bar-g]
P_d (815 ºC) = 2.74 [bar-g]

Finally, considering the ellipsoidal caps, the design pressure calculation depends on its wall thickness and its inside spherical crown radius. From Table UG-37 on page 43 of ASME-BPVC8 [25], the inside spherical crown radius is 90% of the plenum diameter for a 2:1 ellipsoidal cap aspect ratio (see Table A3), or 0.366 m. The ellipsoidal cap wall thickness in Table A3 is greater than 0.2% of this spherical crown radius, so as described in section UG-32(c) on page 28 of ASME-BPVC8 [25], the design pressure may be calculated according to:

$$P_d = \frac{2S_m E_j t_{min}}{D_i + 0.2 t_{min}} \tag{A17}$$

Where

E_j = joint efficiency for, or the efficiency of, appropriate joint in cylindrical or spherical shells, or the efficiency of ligaments between openings, whichever is less.
t_{min} = minimum required thickness of head after forming.

Given that the ellipsoidal cap has no weld joints, the joint efficiency E_j may be taken as 1. Using a conservative estimate of the minimum required thickness of the head after forming to be the same as the nominal wall thickness of the cylindrical tank in Table A3, the resulting design pressures for the ellipsoidal caps at the three temperatures of interest are:

P_d (150 ºC) = 32.1 [bar-g]
P_d (725 ºC) = 6.64 [bar-g]
P_d (815 ºC) = 3.00 [bar-g]

Of the three design pressures, the lowest is that for the longitudinal joints. The tank is stamped and certified by the manufacturer for 30 psig (2.07 bar-g) at 1500 ºF, which is identical to the design pressure calculation for the longitudinal weld joints at the same temperature, which provides a check on the calculations. This design pressure is below the reduced pressure of the venting, so the exhaust plenum would not be appropriate for operation at 1500 ºF. Fortunately, the experiments will not generate temperatures nearly that high, especially under conditions where unburned fuel would accumulate in the exhaust plenum, with temperatures closer to 150 ºC with a safe design pressure of 22.1 bar-g for the longitudinal joints. The highest safe temperature is near 725 ºC, where the safe design pressure is 4.57 bar-g compared to the 4.13 bar-g value of P_{red}. Even this temperature is well outside the range that has ever been experienced in operation of the engine, nor is anticipated for the short experimental runs of the natural gas experiments.

APPENDIX B: INTAKE RUNNER DEFLAGRATION PRESSURE CALCULATIONS

The intake runner may operate at an initial pressure P_0 of up to 2 bar-g. According to Equation A11, the maximum pressure resulting from deflagration starting from an initial pressure P_0 of 2 bar-g is P_{max} = 23.3 bar-g. The effectiveness of venting to achieve a value of P_{red} significantly below P_{max} depends to large degree on the value of the turbulence enhancement factor λ in Equation A1. The value of λ increases with the pipe length, and NFPA68 [24] does not provide specific guidelines for calculating λ for the elevated initial pressure conditions that may be present in the intake runner. Available experimental data for larger diameter (0.4 m) and much longer (30 m) pipes closed at both ends, as is the intake runner when the engine intake valves and check valve at the intake plenum are closed, display an accelerating flame reaching explosion velocities (sum of turbulent flame speed and displacement velocity of expanding burned gases) as high as 36 m/s [38], or 90 times the fundamental burning velocity as the pressure reaches elevated levels due to the confinement of the closed pipe. For such long pipelines, a single burst disk of any reasonable size is unable to reduce P_{red} significantly below P_{max}, such that multiple burst disks each with an area equal to cross-sectional area of the pipe must be employed at appropriate spacing along the entire length of the pipeline, as noted by NFPA68 [24]. Here, however, the relatively short run of the intake runner between the flame arrestor and the intake plenum provides less space and time for so much turbulent flame acceleration. Nevertheless, as a worst-case scenario, an explosion velocity of 36 m/s is a factor of 10 slower than the sonic velocities that flow through a ruptured burst disk (see Equation A12 and associated calculation methods in Appendix A).

Hence, a burst disk with an area roughly a factor of 10 smaller than the cross-sectional area of the intake runner would provide sufficient flow to balance the turbulence-enhanced explosion velocity over the relatively short length of the intake runner. The area of the 1-inch diameter burst disk {202} installed in the intake runner (see Figure 2) is a factor of 10 smaller than the area of the 3.2-inch inner diameter intake runner, so the pressure within the runner would not significantly exceed the burst pressure of 3.1 bar-g. This estimate is admittedly rough, but more precise calculations are not possible because of significant uncertainty due to the lack of established methods for venting design at the elevated pressures and geometry of the intake runner. Despite an exhaustive search of available standards and literature sources, no guidelines could be found that provide more authoritative estimates of the venting requirements for pressurized pipes such as the intake runner.

This estimated pressure developed subsequent to ignition of a worst-case pressurized mixture in the intake runner can be compared to the individual component pressure capacities to assess the integrity of the system. The material of the intake runner piping is 304 stainless steel, similar to the exhaust plenum, and it has a welded longitudinal and circumferential joints. Hence, the same calculations as in Equations A15 and A16 may be used for the intake runner piping at a temperature of 200 ºC, which is the highest anticipated temperature anywhere along the intake runner. Using S_m (200 ºC) = 957 bar [26], E_l = 0.7, E_c = 0.45, D_i = 0.0813 m, and t = 0.00635 m, the design pressures P_d for longitudinal and circumferential weld joints are 48.1 bar and 66.6 bar, respectively. Hence, the intake runner piping is sufficient to withstand the deflagration pressure even without venting.

The class 300 check valve {53} in Figure 2 is rated at above 20 bar-g [22], and the class 150 flanges that join each component of the intake runner are rated for 15.8 bar-g [22]. The

hydrocarbon detector {203} has been tested to 15.5 bar [22], the fuel injector {51} has been tested to 18.4 bar [22], and the flame arrestor {52} has been hydrostatically tested to 10 bar [22]. The strength of the connection of the intake runner to the engine is unknown, but has been reinforced using steel components rather than solely threaded fasteners in the cast iron material of the engine cylinder head. Given that the cylinder head is designed for extended operation intake boost pressures near 3 bar-g, the additional steel reinforcing is likely sufficient to maintain a secure connection between the runner and the cylinder head even if the 3.1 bar-g burst disk ruptures due to an overpressure event.

One other possibility that must be considered is that of a run-up to detonation, which introduces the prospect of a further increase in pressure by a factor of up to three [38]. Fortunately, the low detonation propensity of methane combined with the relatively short length-to-diameter ratio (~25) of the intake runner between the flame arrestor and the intake plenum makes a transition to detonation extremely unlikely [38].

DISTRIBUTION

1	MS0899	Technical Library	9536 (electronic copy)
2	MS0359	D. Chavez, LDRD Office	1911


Sandia National Laboratories